Available online at www.sciencedirect.com
SCIENCE DIRECT®
Coordination Chemistry Reviews 249 (2005) 31–63
COORDINATION CHEMISTRY REVIEWS
www.elsevier.com/locate/ccr

Review

Multiplet effects in X-ray spectroscopy

Frank de Groot*

Department of Inorganic Chemistry and Catalysis, Utrecht University, Sorbonnelaan 16, 3584 CA Utrecht, The Netherlands

Received 29 May 2003; accepted 9 March 2004
Available online 8 July 2004

Contents

---

* Tel.: +31-30-25-36-763; fax: +31-30-25-31-027.
E-mail address: f.m.f.degroot@chem.uu.nl (F. de Groot).
URL: http://www.anorg.chem.uu.nl/people/staff/FrankdeGroot/.

0010-8545/$ – see front matter
doi:10.1016/j.ccr.2004.03.018

Abstract

This review gives an overview of the presence of multiplet effects in X-ray spectroscopy, with an emphasis on X-ray absorption studies on 3d transition metal ions in inorganic oxides and coordination compounds. The first part of the review discusses the basics of multiplet theory and respectively, atomic multiplets, crystal field effects and charge transfer effects are explained. The consequences of 3d-spin–orbit coupling and of 3d systems in symmetries lower than cubic are discussed. The second part of the paper gives a short overview of all X-ray spectroscopies, where the focus is on the multiplet aspects of those spectroscopies and on the various configurations that play a role in combined spectroscopies such as resonant photoemission, resonant X-ray emission and coincidence spectroscopy. The review is concluded with a section that gives an overview of the use of multiplet theory for 3d coordination compounds. Some new developments are sketched, such as the determination of differential orbital covalence and the inclusion of π-(back)bonding.

Keywords: X-ray absorption; X-ray emission; Multiplet theory; Crystal field splitting; Charge transfer

1. Basic aspects of multiplet effects

Multiplet effects play an important role in a large fraction of X-ray and electron spectroscopies. In all cases where a core hole other than a 1 s hole is present in the initial of final state, multiplet effects are important. They determine the spectral shapes and influence the L_3 to L_2 branching ratio.

X-ray absorption spectroscopy (XAS) has become an important tool for the characterization of materials as well as for fundamental studies of atoms, molecules, adsorbates, surfaces, liquids and solids. The particular assets of XAS spectroscopy are its element specificity and the possibility to obtain detailed information without the presence of any long-range order. Below it will be shown that the X-ray absorption spectrum in some cases is closely related to the empty density of states of a system. As such XAS is able to provide a detailed picture of the local electronic structure of the element studied.

1.1. The interaction of X-rays with matter

If an assembly of atoms is exposed to X-rays it will absorb part of the incoming photons. At a certain energy a sharp rise in the absorption is observed (Fig. 1). This sharp rise is called the absorption edge.

The energy of the absorption edge is determined by the binding energy of a core level. Exactly at the edge the photon energy is equal to the binding energy, or more precisely the edge identifies transitions from the ground state to the lowest empty state. Fig. 1 shows the X-ray absorption spectra of manganese and nickel. The $L_{2,3}$ edges relate to a 2p core level and the K edge relates to a 1s core level binding energy.

An X-ray acts on charged particles such as electrons. When an X-ray passes an electron, its electric field pushes the electron first in one direction, then in the opposite direction; in other words, the field oscillates in both direction and strength. The Fermi golden rule states that the transition probability W between a system in its initial state Φ_i and final state Φ_f is given by:

$$W_\mathrm{fi} = \frac{2\pi}{\hbar}|\langle\Phi_\mathrm{f}|T_1|\Phi_\mathrm{i}\rangle|^2\delta_{E_\mathrm{f}-E_\mathrm{i}-\hbar\omega}$$

The delta function takes care of the energy conservation and a transition takes place if the energy of the final state equals the energy of the initial state plus the X-ray energy. The squared matrix element gives the transition rate. The transition operator T_1 describes one-photon transitions such as X-ray absorption. It contains the exponential e^{ikr} describing the electric field. Using a Taylor expansion, this exponential can be approximated as $1 + ikr +$ (higher terms). In case of the K edges from carbon ($Z = 6$, edge = 284 eV) to zinc ($Z = 30$, edge = 9659 eV), the value of $k{\cdot}r$ is $\sim$0.04. The transition probability is equal to the matrix element squared, hence the electric quadrupole transition is smaller by $\sim 2 \times 10^{-3}$ and can be neglected compared to dipole transitions. Rewriting the Fermi golden rule with the dipole approximation gives:

$$W_\mathrm{fi} \propto \sum_q |\langle\Phi_\mathrm{f}|\hat{e}_\mathrm{q}\cdot r|\Phi_\mathrm{i}\rangle|^2\delta_{E_\mathrm{f}-E_\mathrm{i}-\hbar\omega}$$

The Fermi golden rule is a very general expression and uses the initial state (Φ_i) and final state (Φ_f) wave functions. These wave functions are not exactly known and in practical calculations one must make approximations to actually calculate the X-ray absorption cross-section. An often-used

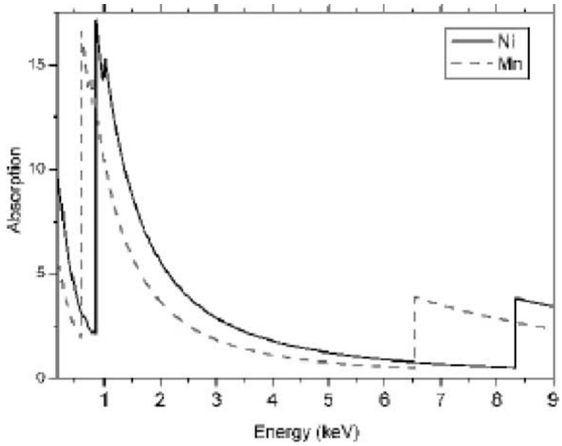

Fig. 1. The X-ray absorption cross-sections of manganese and nickel. Visible are the $L_{2,3}$ edges at, respectively, 680 and 830 eV and the K edges at, respectively, 6500 and 8500 eV.

approximation is the assumption that X-ray absorption is a one-electron process. This single electron (excitation) approximation makes it possible to rewrite the initial state wave function as a core wave function and the final state wave function as a free electron wave function (ε). Hereby one implicitly assumes that all other electrons do not participate in the X-ray induced transition. The matrix element can be rewritten to a single electron matrix element, which often is constant or slowly varying in energy and is abbreviated with the letter M, i.e.:

$$|\langle \Phi_{\mathrm{f}}|\hat{e}_{\mathrm{q}}\cdot\vec{r}|\Phi_{\mathrm{i}}\rangle|^2 = |\langle \Phi_{\mathrm{i}}\underline{c}\varepsilon|\hat{e}_{\mathrm{q}}\cdot\vec{r}|\Phi_{\mathrm{i}}\rangle|^2 \approx |\langle \varepsilon|\hat{e}_{\mathrm{q}}\cdot\vec{r}|c\rangle|^2 \equiv M^2$$

The delta function implies that one observes the density of empty states (ρ) and using the one electron approximation this yields:

$$I_{\mathrm{XAS}} \sim M^2\rho$$

The X-ray absorption selection rules determine that the dipole matrix element M is non-zero if the orbital quantum number of the final state differs by 1 from the initial state ($\Delta L = \pm 1$, i.e. s → p, p → s or d, etc.) and the spin is conserved ($\Delta S = 0$). The quadrupole transitions imply final states that differ by 2 (or 0) from the initial state ($\Delta L = \pm 2$ or 0, i.e. s → d, p → f and s → s, p → p, etc.). They are some hundred times weaker than the dipole transitions and can be neglected in most cases. It will be shown below that they are visible though as pre-edge structures in the K edges of 3d-metals and in the $L_{2,3}$ edges of the rare earths. In the dipole approximation, the shape of the absorption spectrum should look like the partial density of the empty states projected on the absorbing site, convoluted with a Lorentzian (Fig. 2). This Lorentzian broadening is due to the finite lifetime of the core–hole, leading to an uncertainty in its energy according to Heisenberg's uncertainty principle. A more accurate approximation can be obtained if the unperturbed density of states is replaced by the density of states in presence of the core–hole. This approximation gives a relatively adequate simulation of the XAS spectral shape when the interaction between the electrons in the final state is relatively weak. This is often the case for 1s → 4p transitions (the K edges) of the 3d metals.

1.2. The origin of multiplet effects

The single particle description of X-ray absorption works well for all K edges and a range of dedicated computer codes exist to calculate the X-ray absorption cross-section. The review of John Rehr in this issue deals with the latest developments in the single electron codes using multiple scattering [1,2]. Cabaret and co-workers describe the new developments in band structure codes and the recently developed PARATEC-based projection method promises to set a new standard for single electron XANES calculations [3]. Applying these one-electron codes (where one-electron applies to a one-electron core excitation, not to the treatment of the valence electrons) to systems such as transition metal oxides one finds excellent agreement for the metal and oxygen K edges, whereas for the other edges, in particular the metal $L_{2,3}$ edges, the agreement is poor. The reason for this discrepancy is not that the density-of-states is calculated wrongly, but that one does not observe the density of states in such X-ray absorption processes. The reason for the deviation from the density-of-states is the strong overlap of the core wave function with the valence wave functions. The overlap of core and valence wave functions is present also in the ground state, but because all core states are filled, it is not effective and one can approximate the core electrons with their charge. In the final state of an X-ray absorption process one finds a partly filled core state, for example, a $2p^5$ configuration. In case one studies a system with a partly filled 3d-band, for example, NiO, the final state will have an incompletely filled 3d-band. For NiO this can be approximated as a $3d^9$ configuration. The 2p-hole and the 3d-hole have radial wave functions that overlap significantly. This wave function overlap is an atomic effect that can be very large. It creates final states that are found after the vector coupling of the 2p and 3d wave functions. This effect is well known in atomic physics and actually plays a crucial role in the calculation of atomic spectra. Experimentally it was shown that while the direct core hole potential is largely screened, these so-called multiplet effects are hardly screened in the solid state. This implies that the atomic multiplet effects are of the same order of magnitude in atoms and in solids.

Table 1 shows the multiplet interactions between the various possible core holes and the partly filled valence band. The s^1d^9 configurations are calculated for the final states of Ni^{II}, Pd^{II} and Pt^{II}. All s core levels are calculated, for example, in case of Ni^{II} the $1s^13d^9$, $2s^13d^9$ and $3s^13d^9$ configurations, as indicated in Table 1. In case of s core holes, multiplet effects are effectively reduced to just the exchange interaction between the spin of the s core hole and the spin of the valence electrons. The 1s core states have in all cases a very small exchange interaction, implying that multiplet effects will not be visible. This implies that single electron codes will be effective for all K edges (note that for systems that are affected by many body effects, single electron codes are not necessarily correct, but as in X-ray absorption only effects larger than the lifetime broadening, say 0.2 eV or more, are visible, many body effects that cause small energy effects are not visible). The other s-holes have larger

Table 1
The exchange interaction $\langle sd/1/r/sd\rangle$ is given for the final states of Ni^{II}, Pd^{II} and Pt^{II}

	1s	2s	3s	4s	5s
Ni^{II} $c3d^9$	0.07	**5**	**13**		
Pd^{II} $c4d^9$	0.04	2	1	**9**	
Pt^{II} $c5d^9$	0.08	2	1	3	**14**

The valence electrons are the 3d-states for nickel, 4d for palladium and 5d for platinum. The exchange interaction is related to the energy difference of a spin-up and a spin-down core hole due to the interaction with the valence d hole.

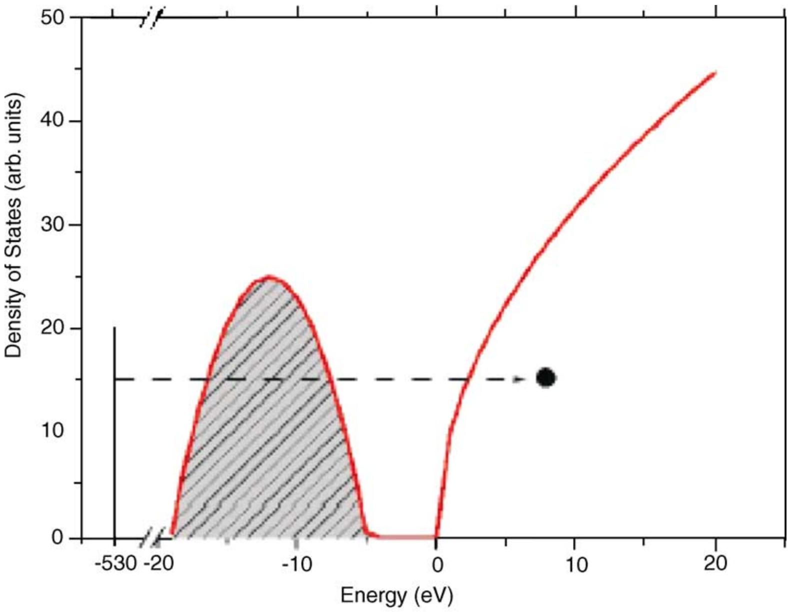

Fig. 2. The schematic density of states of an oxide. The oxygen 1s core electron at 530 eV binding energy is excited to an empty state: the oxygen p-projected density of states.

multiplet effects, implying a splitting of the spectrum. For the core holes given in boldface, this splitting is clearly visible in the actual spectral shapes.

Table 2 shows the multiplet interactions of the p^{5}d^9 and d^{9}d^9 configurations of the final states of Ni^{II} (no d^{9}d^9), Pd^{II} and Pt^{II}, for example, the 2p^{5}5d^9, 3p^{5}5d^9, 4p^{5}5d^9, 5p^{5}5d^9, 3d^{9}5d^9 and 4d^{9}5d^9 configurations for Pt^{II}. For multiplet effects to have a significant effect on the mixing of the L_3 and L_2 edges, the value of the Slater–Condon parameters must be at least of the same order of magnitude as the spin–orbit coupling separating the two edges. If the core spin–orbit coupling is large, there still can be an effect from the Slater–Condon parameters. For example, the 2p and 3p edges of the 4d elements have a large spin–orbit splitting and the multiplet effects are not able to mix states of both sub-edges, but multiplet effects still will affect the spectral shapes [4,5]. If a multiplet effect will actually be visible in X-ray absorption further depends on the respective lifetime broadenings. From the tables it is clear that all shallow core levels are strongly affected and the deeper core levels are less affected. The relatively small multiplet effects for the 2p core levels of the 4d and 5d metals implies that single electron codes, for example, FEFF8, will be effective for the $L_{2,3}$ edges of these systems. The situation for the 3d metals is clear: no visible multiplet effects for the 1s core level (K edge) and a significant influence on all other edges.

Fig. 3 shows the comparison of all edges for Ni^{II} with atomic multiplet effects included. A cubic crystal field of 1.0 eV is included and splits the 3d states. The top three spectra are, respectively, the 1s, 2s and 3s X-ray absorption spectrum calculated as the transition from 1s^{2}3d^{8}4p^0 to 1s^{1}3d^{8}4p^1. The lifetime broadening was set to 0.2 eV

Table 2
The number in the first line for each element indicates the values of the maximum core-valence Slater–Condon parameter for the final states (see text)

	2p	3p	3d	4p	4d	5p
Ni^{II} $\underline{c}$3d^9	**8**	**17**				
	17	**2**				
Pd^{II} $\underline{c}$4d^9	2	7	**10**	**13**		
	160	27	**5**	**5**		
Pt^{II} $\underline{c}$5d^9	3	5	5	10	**10**	**19**
	1710	380	90	90	**17**	**12**

The second line gives the spin–orbit coupling for each core level of Ni^{II}, Pd^{II} and Pt^{II}. Boldface values indicate clearly visible multiplet effects.

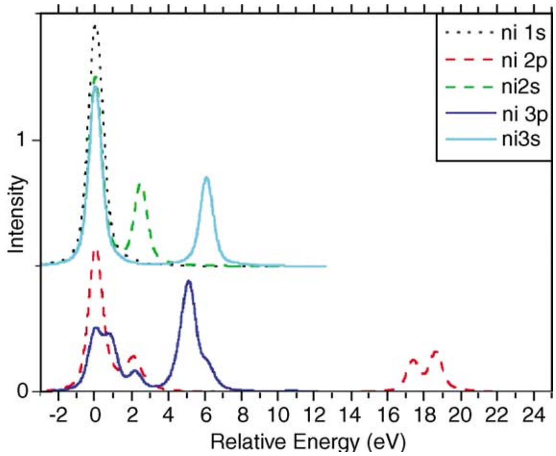

Fig. 3. The X-ray absorption spectra for Ni^{II}. The respective binding energies are 8333, 1008, 870, 110 and 68 eV for the first peak of the 1s, 2s, 2p, 3s and 3p edges.

half-width half-maximum (its actual value is larger for most edges). One observes one peak for the 1s spectrum and two peaks for the 2s and 3s spectra. The reason for the two peaks is the 2s3d and 3s3d exchange interactions. The splittings between the parallel and antiparallel states are ±2.5 and ±6.5 eV, respectively. The actual 1s X-ray absorption spectrum of NiO looks different than a single peak, because one observes an edge jump and transitions from the 1s core state to all empty states of p-character. The complete spectral shape of K edge X-ray absorption is therefore better described with a multiple scattering formalism and this single peak reflects just the first white line or leading edge of the K edge spectrum. The 2s and 3s X-ray absorption spectra are not often studied. The 2s spectrum is very broad and therefore adds little information. The 3s X-ray absorption spectrum is also not very popular, but the 3s core state plays a role in spectroscopies such as 3s XPS, 2p3s resonant X-ray emission, and 2p3s3s resonant Auger [6]. In those spectroscopies the role of the 3s3d exchange interaction plays an important role, as does the charge transfer effect that is discussed below.

The spectra at the bottom of Fig. 3 are the 2p (dashed) and 3p (solid) X-ray absorption spectral shapes. These are the well-known 2p and 3p spectra of NiO and other divalent nickel compounds. The $2p^5 3d^9$ and $3p^5 3d^9$ final states contain one p hole and one 3d hole that interact very strongly. This gives rise to a multitude of final states. Because the lifetime broadening for 2p states is relatively low, its spectral shapes can actually be observed in experiment. This gives 2p X-ray absorption, and to a lesser extend 3p X-ray absorption, their great potential for the determination of the local electronic structure.

A successful method to analyze these transitions is based on a ligand-field multiplet model. For its description, we start with an atomic model, where only the interactions within the absorbing atom are considered, without influence from the surrounding atoms. Solid state effects are then introduced as a perturbation. This can be justified if the intra-atomic interactions are larger than the hybridization effects, which is for example, the case for the 2p and 3p core levels of the 3d systems.

1.3. Atomic multiplets

In order to show how spectra in strongly correlated electron systems are calculated, we start with the example of a free atom, where there is no influence from the environment. The Schrödinger equation contains, respectively, the kinetic energy of the electrons ($p^2/2m$), the electrostatic interaction of the electrons with the nucleus (Ze^2/r), the electron–electron repulsion (e^2/r) and the spin–orbit coupling of each electron ($l{\cdot}s$):

$$H=\sum_N \frac{p_i^2}{2m}+\sum_N \frac{-Ze^2}{r_i}+\sum_{\text{pairs}} \frac{e^2}{r_{ij}}+\sum_N \zeta(r_i) l_i \cdot s_i$$

The first two terms are the same for all electrons in a given atomic configuration and they define the average energy of the configuration (H_{av}). The electron–electron repulsion and the spin–orbit coupling define the relative energy of the different terms within a configuration. The electron–electron repulsion is very large, but the spherical average of the electron–electron interaction can be separated from the non-spherical part. The spherical average is added to H_{av} and the modified electron–electron Hamiltonian H'_{ee} plus H_{ls} determine the energies of the different terms within the atomic configuration.

1.3.1. Term symbols

The terms of a configuration are indicated by their orbital moment L, spin moment S and total moment J, with $|L-S| \leq J \leq L+S$. In the absence of spin–orbit coupling, all terms with the same L and S have the same energy, giving an energy level that is $(2L+1)(2S+1)$-fold degenerate. When spin–orbit coupling is important, the terms are split in energy according to their J-value, each with a degeneracy of $2J+1$. A term is designed with a so-called term symbol $^{2S+1}\mathrm{X}_J$, where X equal to S, P, D and F for L equal to 0, 1, 2 and 3, respectively. A single s electron is given as $^2\mathrm{S}_{1/2}$, a single p electron as $^2\mathrm{P}_{1/2}$ and $^2\mathrm{P}_{3/2}$.

The LS term symbols for a $3d^1 4d^1$ configuration can be directly found by multiplying the term symbols for the individual 3d and 4d electrons. This multiplication consists of separately multiplying L and S of both terms. Since both L and S are vectors, the resulting terms have possible values of $|l_1-l_2| \leq L \leq l_1+l_2$ and $|s_1-s_2| \leq S \leq s_1+s_2$. For $^2\mathrm{D} \otimes {}^2\mathrm{D}$, this gives $L = 0, 1, 2, 3$ or 4 and $S = 0$ or 1. The 10 LS term symbols of the $3d^1 4d^1$ configuration are, respectively, $^1\mathbf{S}$, $^1\mathrm{P}$, $^1\mathbf{D}$, $^1\mathrm{F}$, $^1\mathbf{G}$, $^3\mathrm{S}$, $^3\mathbf{P}$, $^3\mathrm{D}$, $^3\mathbf{F}$ and $^3\mathrm{G}$. In the presence of spin–orbit coupling, a total of 18 term symbols is found.

In the case of a transition metal ion, the configuration of the initial state is $3d^N$. In the final state with, for example, a 2s or a 3p core hole, the configurations are $2s^1 3d^{N+1}$ and $3p^5 3d^{N+1}$. In case of a $3d^2$ configuration, the Pauli exclusion principle forbids two electrons to have the same quantum numbers and 45 combinations are possible, i.e. $10 \times 9/2$. The term symbols are the boldface states of the $3d^1 4d^1$ configuration. In case of a $3d^3$ configuration a similar approach shows that the possible spin-states are doublet and quartet. The quartet-states have all spins parallel and the Pauli exclusion principle implies that there are two quartet term symbols, respectively, $^4\mathrm{F}$ and $^4\mathrm{P}$. The doublet states have two electrons parallel and for these two electrons the Pauli principle yields the combinations identical to the triplet states of the $3d^2$ configuration. To these two parallel electrons a third electron is added anti-parallel, where this third electron can have any value of its orbital quantum number m_l. Writing out all combinations and separating them into the total orbital moments M_l gives the doublet term symbols $^2\mathrm{H}$, $^2\mathrm{G}$, $^2\mathrm{F}$, $^2\mathrm{D}$, another $^2\mathrm{D}$ and $^2\mathrm{P}$. By adding the degeneracies, it can be checked that a $3d^3$ configuration has 120 different states, i.e.

$10 \times 9/2 \times 8/3$. Because there is a symmetry equivalence of holes and electrons, the pairs $3d^2$–$3d^8$, $3d^3$–$3d^7$, etc. have exactly the same term symbols. The general formula to determine the degeneracy of a $3d^N$ configuration is:

$$\binom{10}{N} = \frac{10!}{(10-N)!N!}$$

The 2p X-ray absorption edge (2p → 3d transition) is often studied for the 3d transition metal series, and it provides a wealth of information. Crucial for its understanding are the configurations of the $2p^5 3d^N$ final states. The term symbols of the $2p^5 3d^N$ states are found by multiplying the configurations of $3d^N$ with a ^2P term symbol. The total degeneracy of a $2p^5 3d^N$ state is six times the degeneracy of $3d^N$. For example, a $2p^5 3d^5$ configuration has 1512 possible states. Analysis shows that these 1512 states are divided into 205 term symbols, implying in principle 205 possible final states. Whether all these final states actually have finite intensity depends on the selection rules.

1.3.2. Matrix elements

The term symbol of a $3d^N$ configuration describes the symmetry aspects, but it does not say anything about its relative energy. The relative energies of the different terms are determined by calculating the matrix elements of these states with the effective electron–electron interaction H'_{ee} and the spin–orbit coupling H_{ls}. The general formulation of the matrix elements of the effective electron–electron interaction is given as:

$$\left\langle {}^{2S+1}L_J \left| \frac{e^2}{r_{12}} \right| {}^{2S+1}L_J \right\rangle = \sum_k f_k F^k + \sum_k g_k G^k$$

$F^i(f_i)$ and $G^i(g_i)$ are the Slater–Condon parameters for, respectively, the radial (angular) part of the direct Coulomb repulsion and the Coulomb exchange interaction. f_i and g_i are non-zero only for certain values of i, depending on the configuration. The direct Coulomb repulsion f_0 is always present and the maximum value for i equals two times the lowest value of l. The exchange interaction g_i is present only for electrons in different shells. For g_k, i is even if $l_1 + l_2$ is even, and i is odd if $l_1 + l_2$ is odd. The maximum value of i equals $l_1 + l_2$. For 3d-states, it is important to note that a $3d^N$ configuration contains f_0, f_2 and f_4 Slater–Condon parameters. The final state $2p^5 3d^{N+1}$ configuration contains f_0, f_2, f_4, g_1, and g_3 Slater–Condon parameters.

For a $3d^2$ configuration, we found the five term symbols ^1S, ^3P, ^1D, ^3F and ^1G. f_0 is equal to the number of pairs $N(N-1)/2$ of N electrons, i.e. it is equal to 1 for two electrons. The Slater–Condon parameters F^2 and F^4 have approximately a constant ratio: $F^4 = 0.62$, F^2. In case of the 3d transition metal ions, F^2 is approximately equal to 10 eV. This gives for the five term symbols of the $3d^2$ configuration, respectively, ^3F at −1.8 eV, ^1D at −0.1 eV, ^3P at +0.2 eV, ^1G at +0.8 eV and ^1S at +4.6 eV. The ^3F term symbol has the lowest energy and it is the ground state of a $3d^2$ system. This is a confirmation of the Hunds rules, which will be discussed below. The three states ^1D, ^3P and ^1G are close in energy some 1.7–2.5 eV above the ground state. The ^1S state has a high energy of 6.4 eV above the ground state, the reason being that two electrons in the same orbital strongly repel each other.

For three and more electrons the situation is considerably more complex. It is not straightforward to write down an anti-symmetrized three-electron wave function. It can be shown that the three-electron wave function can be built from two-electron wave functions with the use of the so-called *coefficients of fractional parentage*. For a partly filled d-band, the term symbol with the lowest energy is given by the so-called Hunds rules. Based on experimental information Hund formulated three rules to determine the ground state of a $3d^N$ configuration. The three Hunds rules are the following.

1. Term symbols with maximum spin S are lowest in energy.
2. Among these terms, the one with the maximum orbital moment L is lowest.
3. In the presence of spin–orbit coupling, the lowest term has $J = |L - S|$ if the shell is less than half full and $J = L + S$ if the shell is more than half full.

A configuration has the lowest energy if the electrons are as far apart as possible. The first Hunds rule ‘maximum spin’ can be understood from the Pauli principle: electrons with parallel spins must be in different orbitals, which on overall implies larger separations, hence lower energies. This is for example, evident for a $3d^5$ configuration, where the ^6S state has its five electrons divided over the five spin-up orbitals, which minimizes their repulsion. In case of $3d^2$, the second Hunds rule implies that the ^3F term symbol is lower than the ^3P-term symbol, because the ^3F wave function tends to minimize electron repulsion.

1.3.3. X-ray absorption spectra described with atomic multiplets

We start with the description of closed shell systems. The 2p X-ray absorption process excites a 2p core electron into the empty 3d shell and the transition can be described as $2p^6 3d^0 \rightarrow 2p^5 3d^1$. The ground state has $^1S_0$ symmetry and we find that the term symbols of the final state are $^1P_1$, $^1D_2$, $^1F_3$, $^3P_{012}$, $^3D_{123}$ and $^3F_{234}$. The energies of the final states are affected by the 2p3d Slater–Condon parameters, the 2p spin–orbit coupling and the 3d spin–orbit coupling. The X-ray absorption transition matrix elements to be calculated are:

$$I_{XAS} \propto \langle 3d^0_{[^1S_0]} | \vec{r}_{[^1P_1]} | 2p^5 3d^1_{[^{1,3}PDF]} \rangle^2$$

The 12 final states are built from the 12 term symbols, with the restriction that the states with the same J-value block out in the calculation. The symmetry of the dipole transition is given as $^1P_1$, according to the dipole selection rules, which state that $\Delta J = \pm 1$ or 0, with the exception of

$J' = J = 0$. Within LS coupling also $\Delta S = 0$ and $\Delta L = 1$. The dipole selection rule reduces the number of final states that can be reached from the ground state. The *J*-value in the ground state is zero, proclaiming that the *J*-value in the final state must be one, thus only the three term symbols $^1P_1$, $^3P_1$ and $^3D_1$ obtain finite intensity. The problem of calculating the 2p absorption spectrum is hereby reduced to solving the 3×3 energy matrix of the final states with $J = 1$.

To indicate the application of this simple calculation, we compare a series of X-ray absorption spectra of tetravalent titanium 2p and 3p edges and the trivalent lanthanum 3d and 4d edges. The ground states of Ti^{IV} and La^{III} are, respectively, 3d^0 and 4f^0 and they share a ^{1}S ground state. The transitions at the four edges are, respectively, $3d^0 \rightarrow 2p^5 3d^1$, $3d^0 \rightarrow 3p^5 3d^1$, $4f^0 \rightarrow 3d^9 4f^1$ and $4f^0 \rightarrow 4d^9 4f^1$. These four calculations are equivalent and all spectra consist of three peaks. What changes are the values of the atomic Slater–Condon parameters and core hole spin–orbit couplings, as given in table. The important factor for the spectral shape is the ratio of the core spin–orbit coupling and the F^2 value. Finite values of both the core spin–orbit and the Slater–Condon parameters cause the presence of the pre-peak. It can be seen in Table 3 that the 3p and 4d spectra have small core spin–orbit couplings, implying small $p_{3/2}$ ($d_{5/2}$) edges and extremely small pre-peak intensities. The deeper 2p and 3d core levels have larger core spin–orbit splitting with the result of a $p_{3/2}$ ($d_{5/2}$) edge of almost the same intensity as the $p_{1/2}$ ($d_{3/2}$) edge and a larger pre-peak. Note that none of these systems comes close to the single-particle result of a 2:1 ratio of the p edges or the 3:2 ratio of the d edges. Fig. 4 shows the X-ray absorption spectral shapes. They are given on a logarithmic scale to make the pre-edges visible.

Table 3
The relative intensities, energy, core hole spin–orbit coupling and F^2 Slater–Condon parameters are compared for four different $^1S_0$ systems

Edge	Ti 2p	Ti 3p	La 3d	La 4d
Average energy (eV)	464.00	37.00	841.00	103.00
Core spin–orbit (eV)	3.78	0.43	6.80	1.12
F^2 Slater–Condon (eV)	5.04	8.91	5.65	10.45
Intensities				
Pre-peak	0.01	10^{-4}	0.01	10^{-3}
$p_{3/2}$ or $d_{5/2}$	0.72	10^{-3}	0.80	0.01
$p_{1/2}$ or $d_{3/2}$	1.26	1.99	1.19	1.99

The G^1 and G^3 Slater–Condon parameters have an approximately constant ratio with respect to the F^2 value.

In Table 4 the ground state term symbols of all 3d^N systems are given. Together with the dipole selection rules this strongly limits the number of final states that can be reached. Consider, for example, the $3d^3 \rightarrow 2p^5 3d^4$ transition: The 3d^3 ground state has $J = 3/2$ and there are, respectively, 21, 35 and 39 terms of the 2p^{5}3d^4 configuration with $J' = 1/2$, 3/2 and 5/2. This implies a total of 95 allowed peaks out of the 180 final state term symbols. From Table 4 some special cases can be found, for example, a 3d^9 system makes a transition to a 2p^{5}3d^{10} configuration, which has only two term symbols, out of which only the term symbol with $J' = 3/2$ is allowed. In other words, the L$_2$ edge has zero intensity. The 3d^0 and 3d^8 systems have only three, respectively, four peaks, because of the limited amount of states for the 2p^{5}3d^1 and 2p^{5}3d^9 configurations.

Atomic multiplet theory is able to accurately describe the 3d and 4d X-ray absorption spectra of the rare earths. In case of the 3d metal ions, atomic multiplet theory can not simulate the X-ray absorption spectra accurately because the

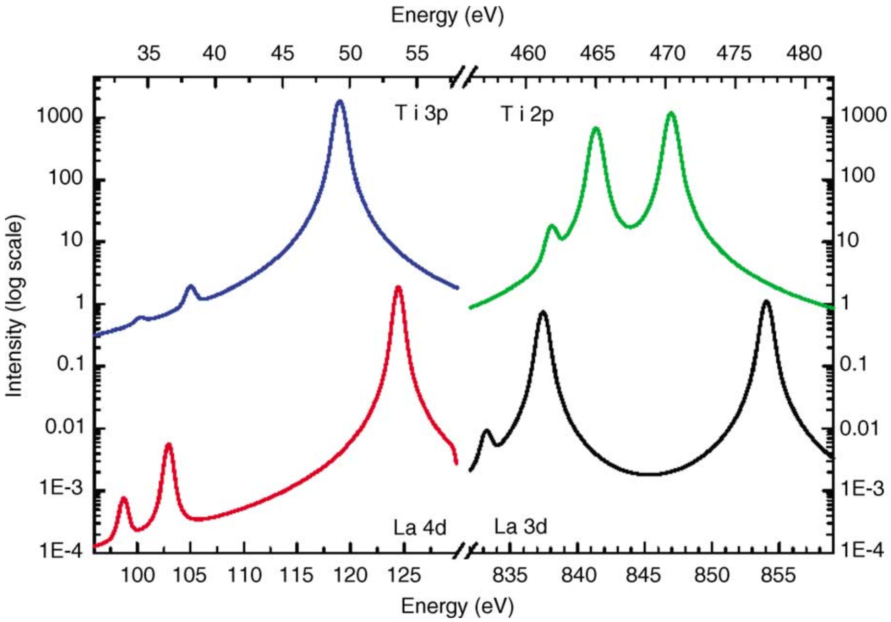

Fig. 4. The La^{III} 4d and 3d plus T^{IIV} 3p and 2p X-ray absorption spectra as calculated for isolated ions. The intensity is given on a logarithmic scale to make the pre-edge peaks visible. The intensities of titanium have been multiplied by 1000.

Table 4
The 2p X-ray absorption transitions from the atomic ground state to all allowed final state symmetries, after applying the dipole selection rule: $\Delta J = -1$, 0 or $+1$

Transition	Ground	Transitions	Term symbols
$3d^0 \rightarrow 2p^5 3d^1$	$^1S_0$	3	12
$3d^1 \rightarrow 2p^5 3d^2$	$^2D_{3/2}$	29	45
$3d^2 \rightarrow 2p^5 3d^3$	$^3F_2$	68	110
$3d^3 \rightarrow 2p^5 3d^4$	$^4F_{3/2}$	95	180
$3d^4 \rightarrow 2p^5 3d^5$	$^5D_0$	32	205
$3d^5 \rightarrow 2p^5 3d^6$	$^6S_{5/2}$	110	180
$3d^6 \rightarrow 2p^5 3d^7$	$^5D_2$	68	110
$3d^7 \rightarrow 2p^5 3d^8$	$^4F_{9/2}$	16	45
$3d^8 \rightarrow 2p^5 3d^9$	$^3F_4$	4	12
$3d^9 \rightarrow 2p^5 3d^{10}$	$^2D_{5/2}$	1	2

effects of the neighbors are too large. It turns out that it is necessary to include explicitly both the symmetry effects and the configuration–interaction effects of the neighbors. Ligand field multiplet theory takes care of all symmetry effects, while charge transfer multiplet theory allows the use of more than one configuration.

1.4. The crystal field multiplet model

Crystal field theory is a well-known model used to explain the electronic properties of transition metal systems. It was developed in the fifties and sixties, mainly against a background of explaining optical spectra and EPR data. The starting point of the crystal field model is to approximate the transition metal as an isolated atom surrounded by a distribution of charges that should mimic the system, molecule or solid, around the transition metal. At first sight, this is a very simplistic model and one might doubt its usefulness to explain experimental data. However it turned out that such a simple model was extremely successful to explain a large range of experiments, like optical spectra, EPR spectra, magnetic moments, etc.

Maybe the most important reason for the success of the crystal field model is that the properties explained are strongly determined by symmetry considerations. With its simplicity in concept, the crystal field model could make full use of the results of group theory. Group theory also made possible a close link to atomic multiplet theory. Group theoretically speaking, the only thing crystal field theory does is translate, or branch, the results obtained in atomic symmetry to cubic symmetry and further to any other lower point groups. The mathematical concepts for these branchings are well developed [7,8]. In this chapter we will use these group theoretical results and study their effects on the ground states as well as on the spectral shapes.

The crystal field multiplet Hamiltonian extends the atomic Hamiltonian with an electrostatic field. The electrostatic field consists of the electronic charge e times a potential that describes the surroundings. This potential $\phi(r)$ is written as a series expansion of spherical harmonics Y_{LM}'s:

$$\phi(r) = \sum_{L=0}^{\infty} \sum_{M=-L}^{L} r^L A_{\mathrm{LM}} Y_{\mathrm{LM}}(\psi, \phi)$$

The crystal field is regarded as a perturbation to the atomic result. This implies that it is necessary to determine the matrix elements of $\phi(r)$ with respect to the atomic 3d orbitals $\langle 3d|\phi(r)|3d\rangle$. One can separate the matrix elements into a spherical part and a radial part, as was done also for the atomic Hamiltonian. The radial part of the matrix elements yields the strength of the crystal field interaction. The spherical part of the matrix element can be written in Y_{LM} symmetry, which limits the crystal field potential for 3d electrons to:

$$\phi(r) = A_{00}Y_{00} + \sum_{M=-2}^{2} r^2 A_{2M} Y_{2M} + \sum_{M=-4}^{4} r^4 A_{4M} Y_{4M}$$

The first term $A_{00}Y_{00}$ is a constant. It will only shift the atomic states and it is not necessary to include this term explicitly if one calculates the spectral shape.

1.4.1. Cubic crystal fields

A large range of systems consist of a transition metal ion surrounded by six neighboring atoms, where these neighbors are positioned on the three Cartesian axes, or in other words, on the six faces of a cube surrounding the transition metal. They form a so-called octahedral field, which belongs to the O_h point group. The calculation of the X-ray absorption spectral shape in atomic symmetry involved the calculation of the matrices of the initial state, the final state and the transition. The initial state is given by the matrix element $\langle 3d^N|H_{\mathrm{ATOM}}|3d^N\rangle$, which for a particular J-value in the initial state gives $\sum_J \langle J|0|J\rangle$. The same applies for the final state matrix element and the dipole matrix element. To calculate the X-ray absorption spectrum in a cubic crystal field, these atomic matrix elements must be branched to cubic symmetry.

The symmetry change from spherical symmetry (SO_3) to octahedral symmetry (O_h) causes the S and P symmetry states to branch, respectively, to an A_{1g} and a T_{1u} symmetry state. A D symmetry state branches to E_g plus T_{2g} symmetry states in octahedral symmetry and an F symmetry state to $A_{2u} + T_{1u} + T_{2u}$. One can make the following observations: The dipole transition operator has p-symmetry and is branched to T_{1u} symmetry, implying that there will be no dipolar angular dependence in O_h symmetry. The quadrupole transition operator has d-symmetry and is split into two operators in O_h symmetry, in other words, there will be different quadrupole transitions in different directions.

In a similar way, the symmetry can be changed from octahedral O_h to tetragonal D_{4h}, with the corresponding description with a branching table. An atomic s-orbital is branched to D_{4h} symmetry according to the branching series $S \rightarrow A_{1g} \rightarrow A_{1g}$, i.e. it will always remain the unity element in all symmetries. An atomic p-orbital is branched

Table 5
The energy of the 3d orbitals is expressed in X_{400}, X_{420} and X_{220} in the second column and in Dq, Ds and Dt in the third column

Γ	Energy expressed in X-terms	Energy in D-terms	Orbitals
b_1	$1/\sqrt{30}\cdot X_{400} - 1/\sqrt{42}\cdot X_{420} - 2/\sqrt{70}\cdot X_{220}$	6Dq + 2Ds − 1Dt	$3d_{x2-y2}$
a_1	$1/\sqrt{30}\cdot X_{400} + 1/\sqrt{42}\cdot X_{420} + 2/\sqrt{70}\cdot X_{220}$	6Dq − 2Ds − 6Dt	$3d_{z2}$
b_2	$-2/3\sqrt{30}\cdot X_{400} + 4/3\sqrt{42}\cdot X_{420} - 2/\sqrt{70}\cdot X_{220}$	−4Dq + 2Ds − 1Dt	$3d_{xy}$
e	$-2/3\sqrt{30}\cdot X_{400} - 2/3\sqrt{42}\cdot X_{420} + 1/\sqrt{70}\cdot X_{220}$	−4Dq − 1Ds + 4Dt	$3d_{xz}$, $3d_{yz}$

according to P → T_{1u} → $E_u + A_{2u}$. The dipole transition operator has p-symmetry and hence is branched to $E_u + A_{2u}$ symmetry, in other words, the dipole operator is described with two operators in two different directions implying an angular dependence in the X-ray absorption intensity. A D-state is branched according to $D \rightarrow E_g + T_{2g} \rightarrow A_{1g} + B_{1g} + E_g + B_{2g}$, etc. The Hamiltonian is given by the unity representation A_{1g}. Similarly as in O_h symmetry, the atomic G-symmetry state branches into the Hamiltonian in D_{4h} symmetry according to the series $G \rightarrow A_{1g} \rightarrow A_{1g}$. In addition, it can be seen that the E_g symmetry state of O_h symmetry branches to the A_{1g} symmetry state in D_{4h} symmetry. The E_g symmetry state in O_h symmetry is found from the D and G atomic states. This implies that also the series $G \rightarrow E_g \rightarrow A_{1g}$ and $D \rightarrow E_g \rightarrow A_{1g}$ become part of the Hamiltonian in D_{4h} symmetry. We find that the second term $A_{2M}Y_{2M}$ is part of the Hamiltonian in D_{4h} symmetry. The three branching series in D_{4h} symmetry are in Butlers notation given as $4 \rightarrow 0 \rightarrow 0, 4 \rightarrow 2 \rightarrow 0$ and $2 \rightarrow 2 \rightarrow 0$ and the radial parameters related to these branches are indicated as X_{400}, X_{420}, and X_{220}. The X_{400} term is important already in O_h symmetry. This term is closely related to the cubic crystal field term 10Dq as will be discussed below.

1.4.2. The definitions of the crystal field parameters

In order to compare the X_{400}, X_{420}, and X_{220} crystal field operators to other definitions, for example, Dq, Ds, Dt, we compare their effects on the set of 3d-functions. The most straightforward way to specify the strength of the crystal field parameters is to calculate the energy separations of the 3d-functions. In O_h symmetry there is only one crystal field parameter X_{40}. This parameter is normalized in a manner that creates unitary transformations in the calculations. The result is that it is equal to $1/18 \times \sqrt{30}$ times 10Dq, or 0.304 times10Dq. In tetragonal symmetry (D_{4h}) the crystal field is given by three parameters, X_{400}, X_{420} and X_{220}. An equivalent description is to use the parameters Dq, Ds and Dt. Table 5 gives the action of the X_{400}, X_{420} and X_{220} on the 3d-orbitals and relates the respective symmetries to the linear combination of X parameters, the linear combination of the Dq, Ds and Dt parameters and the specific 3d-orbital of that particular symmetry.

Table 5 implies that one can write X_{400} as a function of Dq and Dt, i.e. $X_{400} = 6 \times 30^{1/2} \times \text{Dq} - 7/2 \times 30^{1/2} \times \text{Dt}$. In addition, it is found that $X_{420} = -5/2 \times 42^{1/2} \times \text{Dt}$ and $X_{220} = -70^{1/2} \times \text{Ds}$. These relations allow the quick transfer from, for example, the values of Dq, Ds and Dt from optical spectroscopy to these X-values as used in X-ray absorption.

1.4.3. The energies of the $3d^N$ configurations

We will use the $3d^8$ configuration as an example to show the effects of O_h and D_{4h} symmetry. Assuming for the moment that the 3d spin–orbit coupling is zero, in O_h symmetry the five term symbols of $3d^8$ in spherical symmetry split into eleven term symbols. Their respective energies can be calculated by adding the effect of the cubic crystal field 10Dq to the atomic energies. The diagrams of the respective energies with respect to the cubic crystal field are known as the Tanabe–Sugano diagrams. Fig. 5 gives the Tanabe–Sugano diagram for the $3d^8$ configuration. The ground state of a $3d^8$ configuration in O_h symmetry has $^3A_{2g}$ symmetry and is set to zero energy. If the crystal field energy is 0.0 eV, one has effectively the atomic multiplet states. From low energy to high energy, one can observe, respectively, the ^3F, ^1D, ^3P, ^1G and ^1S states. Including a finite crystal field strength splits these states, for example, the ^3F state is split

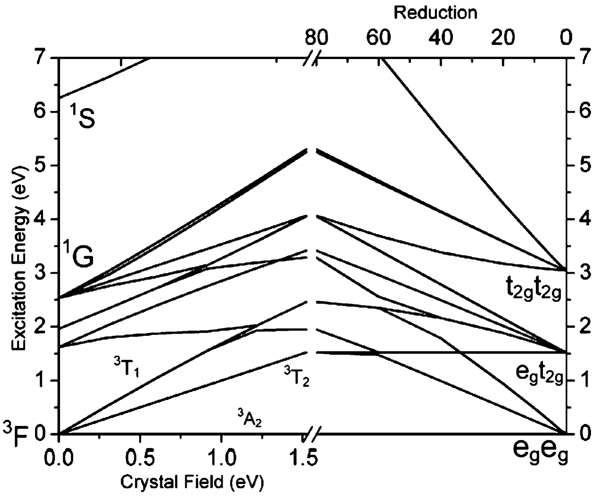

Fig. 5. The Tanabe–Sugano diagram for a $3d^8$ configuration in O_h symmetry. The atomic states of a $3d^8$ configuration are split by electrostatic interactions into the ^3F ground state, the ^1D and ^3P states (at ∼2 eV), the ^1G state (at ∼2.5 eV) and the ^1S state (at ∼6 eV), for which atomic Slater–Condon parameters have been used, which relates to 80% of the Hartree–Fock value [12,15]. The horizontal axis gives the crystal field in eV. On the right half of the figure the Slater–Condon parameters are reduced from their atomic values (80%) to zero. In case all Slater–Condon parameters are zero, there are only three states possible related to, respectively, the ground state with two holes in e_g states, a e_g hole plus a t_{2g} hole at exactly 10Dq and two t_{2g} holes at two times 10Dq.

Table 6
The high-spin and low-spin distribution of the 3d electrons for the configurations $3d^4$ to $3d^7$

Configurations	High-spin	Low-spin	10Dq (D)	Exchange (J)	J/D
$3d^4$	$t^3_{2g+}e^1_{g+}$	$t^3_{2g+}t^1_{2g-}$	1D	$3J_{te}$	3
$3d^5$	$t^3_{2g+}e^2_{g+}$	$t^3_{2g+}t^2_{2g-}$	2D	$6J_{te} + J_{ee} - J_{tt}$	~3
$3d^6$	$t^3_{2g+}e^2_{g+}t^1_{2g-}$	$t^3_{2g+}t^3_{2g-}$	2D	$6J_{te} + J_{ee} - 3J_{tt}$	~2
$3d^7$	$t^3_{2g+}e^2_{g+}t^2_{2g-}$	$t^3_{2g+}t^3_{2g-}e^1_{g+}$	1D	$3J_{te} + J_{ee} - 2J_{tt}$	~2

The fourth column gives the difference in crystal field energy, the fifth column the difference in exchange energy. For the last column, we have assumed that $J_{te} \sim J_{ee} \sim J_{tt} = J$.

into $^3A_{2g} + {}^3T_{1g} + {}^3T_{2g}$, following the branching rules as described above. At higher crystal field strengths states start to change their order and they cross. Whether states actually cross each other or show non-crossing behavior depends on whether their symmetries allow them to form a linear combination of states. This also depends on the inclusion of the 3d spin–orbit coupling. The right part of the figure shows the effect of the reduction of the Slater–Condon parameters. For a crystal field of 1.5 eV the Slater–Condon parameters were reduced from their atomic value, indicated with 80% of their Hartree–Fock value to 0%. The spectrum for 0% has all its Slater–Condon parameters reduced to zero, In other words, the 3d3d coupling has been turned of and one observes the energies of two non-interacting 3d-holes. This single particle limit has three configurations, respectively, the two holes in e_ge_g, e_gt_{2g} and $t_{2g}t_{2g}$ states. The energy difference between e_ge_g and e_gt_{2g} is exactly the crystal field value of 1.5 eV. This figure shows nicely the transition from the single particle picture to the multiplet picture for the $3d^8$ ground state.

The ground state of a $3d^8$ configuration in O_h symmetry always remains $^3A_{2g}$. The reason is clear if one compares these configurations to the single particle description of a $3d^8$ configuration. In a single particle description a $3d^8$ configuration is split by the cubic crystal field into the t_{2g} and the e_g configuration. The t_{2g} configuration has the lowest energy and can contain six 3d electrons. The remaining two electrons are placed in the e_g configuration, where both have a parallel alignment according to Hunds rule. The result is that the overall configuration is ${t_{2g}}^6{e_{g+}}^2$. This configuration identifies with the $^3A_{2g}$ configuration.

Both configurations e_g and t_{2g} can split by the Stoner exchange splitting J. This Stoner exchange splitting J is given as a linear combination of the Slater–Condon parameters as $J = (F_2 + F_4)/14$ and it is an approximation to the effects of the Slater–Condon parameters and in fact, a second parameter C, the orbital polarization, can be used in combination with J. The orbital polarization C is given as $C = ({}^9F_2 - {}^5F_4)/98$. We assume for the moment that the effect of the orbital polarization will not modify the ground states. In that case, the (high-spin) ground states of $3d^N$ configurations are simply given by filling, respectively, the t_{2g+}, e_{g+}, t_{2g-} and e_{g-} states. For example, the $^4A_{2g}$ ground state of $3d^3$ is simplified as t^3_{2g+} and the $^3A_{2g}$ ground state of $3d^8$ as $t^3_{2g+}{e_{g+}}^2t^3_{2g-}$, etc.

For the configurations $3d^4$, $3d^5$, $3d^6$ and $3d^7$ there are two possible ground state configurations in O_h symmetry. A high-spin ground state that originates from the Hunds rule ground state and a low-spin ground state for which first all t_{2g} levels are filled. The transition point from high-spin to low-spin ground states is determined by the cubic crystal field 10Dq and the exchange splitting J. The exchange splitting is present for every two parallel electrons. Table 6 gives the high-spin and low-spin occupations of the t_{2g} and e_g spin-up and spin-down orbitals t_{2g+}, e_{g+}, t_{2g-} and e_{g-}. The $3d^4$ and $3d^7$ configuration differ by one t_{2g} versus e_g electron hence exactly the crystal field splitting D. The $3d^5$ and $3d^6$ configurations differ by 2D. The exchange interaction J is slightly different for e_ge_g, e_gt_{2g} and $t_{2g}t_{2g}$ interactions and the fifth column contains the overall exchange interactions. The last column can be used to estimate the transition point. For this estimate the exchange splittings were assumed to be equal, yielding the simple rules that for $3d^4$ and $3d^5$ configurations high-spin states are found if the crystal field splitting is less than $3J$. In case of $3d^6$ and $3d^7$ configurations the crystal field value should be less than $2J$ for a high-spin configuration. Because J can be estimated as 0.8 eV, the transition points are approximately 2.4 eV for $3d^4$ and $3d^5$, respectively, 1.6 eV for $3d^6$ and $3d^7$. In other words, $3d^6$ and $3d^7$ materials have a tendency to be low-spin compounds. This is particularly true for $3d^6$ compounds because of the additional stabilizing nature of the $3d^6$ $^1A_{1g}$ low spin ground state.

1.4.4. Symmetry effects in D_{4h} symmetry

In D_{4h} symmetry the t_{2g} and e_g symmetry states split further into e_g and b_{2g}, respectively, a_{1g} and b_{1g}. Depending on the nature of the tetragonal distortion either the e_g or the b_{2g} state have the lowest energy. All configurations from $3d^2$ to $3d^8$ have a low-spin possibility in D_{4h} symmetry. Only the $3d^2$ configuration with the e_g state as ground state does not possess a low-spin configuration. The $3d^1$ and $3d^9$ configurations contain only one unpaired spin thus they have no possibility to form a low-spin ground state. It is important to note that a $3d^8$ configuration as, for example, found in Ni^{II} and Cu^{III} can yield a low-spin configuration. Actually this low-spin configuration is found in the trivalent parent compounds of the high T_C superconducting oxides [9,10]. The D_{4h} symmetry ground states are particularly important for

Table 7
The branching of the spin-symmetry states and its consequence on the states that are found after the inclusion of spin–orbit coupling

Configurations	Ground state in SO_3	HS ground state in O_h	Spin in O_h	Degree	Overall symmetry in O_h
$3d^0$	$^1S_0$	$^1A_{1g}$	A_{1g}	1	A_{1g}
$3d^1$	$^2D_{3/2}$	$^2T_{2g}$	E_{2g}	2	$E_{1g} + G_g$
$3d^2$	$^3F_2$	$^3T_{1g}$	T_{1g}	4	$E_g + T_{1g} + T_{2g} + A_{1g}$
$3d^3$	$^4F_{3/2}$	$^4A_{2g}$	G_g	1	G_g
$3d^4$	$^5D_0$	^5E_g	$E_g + T_{2g}$	5	$A_{1g} + A_{2g} + Eg + T_{1g} + T_{2g}$
		$^3T_{1g}$	T_{1g}	4	$Eg + T_{1g} + T_{2g} + A_{1g}$
$3d^5$	$^6S_{5/2}$	$^6A_{1g}$	$G_g + E_{1g}$	2	$G_g + E_{1g}$
		$^2T_{2g}$	E_{2g}	2	$G_g + E_{1g}$
$3d^6$	$^5D_2$	$^5T_{2g}$	$E_g + T_{2g}$	6	$A_{1g} + E_g + T_{1g} + T_{1g} + T_{2g} + T_{2g}$
		$^1A_{1g}$	A_{1g}	1	A_{1g}
$3d^7$	$^4F_{9/2}$	$^4T_{1g}$	G_g	4	$E_{1g} + E_{2g} + G_g + G_g$
		^2E_g	E_{2g}	1	G_g
$3d^8$	$^3F_4$	$^3A_{2g}$	T_{1g}	1	T_{2g}
$3d^9$	$^2D_{5/2}$	^2E_g	E_{2g}	1	G_g

The fourth column gives the spin-projection and the fifth column its degeneracy. The last column lists all the symmetry states after inclusion of spin–orbit coupling.

those cases where O_h symmetry yields a half-filled e_g state. This is the case for $3d^4$ and $3d^9$ plus low-spin $3d^7$. These ground states are unstable in octahedral symmetry and will relax to, for example, a D_{4h} ground state, the well-known Jahn-Teller distortion. This yields the Cu^{II} ions with all states filled except the $^1A_{1g}$-hole.

1.4.5. The effect of the 3d spin–orbit coupling

As discussed above the inclusion of 3d spin–orbit coupling will bring one to the multiplication of the spin and orbital moments to a total moment. In this process one loses the familiar nomenclature for the ground states of the $3d^N$ configurations. In total symmetry also the spin moments are branched to the same symmetry group as the orbital moments, yielding for NiO a $^3A_{2g}$ ground state with an overall ground state of $T_{1g} \otimes A_{2g} = T_{2g}$. It turns out that in many solids it is better to omit the 3d spin–orbit coupling because it is effectively 'quenched'. This was found to be the case for CrO_2. A different situation is found for CoO, where the explicit inclusion of the 3d spin–orbit coupling is essential for a good description of the 2p X-ray absorption spectral shape. In other words, 2p X-ray absorption is able to determine the different role of the 3d spin–orbit coupling in, respectively, CrO_2 (quenched) and CoO (not quenched).

Table 7 gives the spin-projection to O_h symmetry. The ground states with an odd number of 3d electrons have a ground state spin moment that is half-integer [7,11]. Table 7 shows that the degeneracy of the overall symmetry states is often not exactly equal to the spin number as given in the third column. For example, the $^3T_{1g}$ ground state is split into four configurations, not three as one would expect. If the 3d spin–orbit coupling is small (and if no other state is close in energy), two of these four states are quasi-degenerate and one finds three states. This is in general the case for all situations. Note that the $^6A_{1g}$ ground state of $3d^5$ is split into two configurations. These configurations are degenerate as far as the 3d spin–orbit coupling is concerned. However because of differences in the mixing of excited term symbols a small energy difference can be found. This is the origin of the small but non-zero zero field splitting in the EPR analysis of $3d^5$ compounds.

Fig. 6 shows the Tanabe–Sugano diagram for a $3d^7$ configuration in O_h symmetry. Only the excitation energies from 0.0 to 0.4 eV are shown to highlight the high-spin to

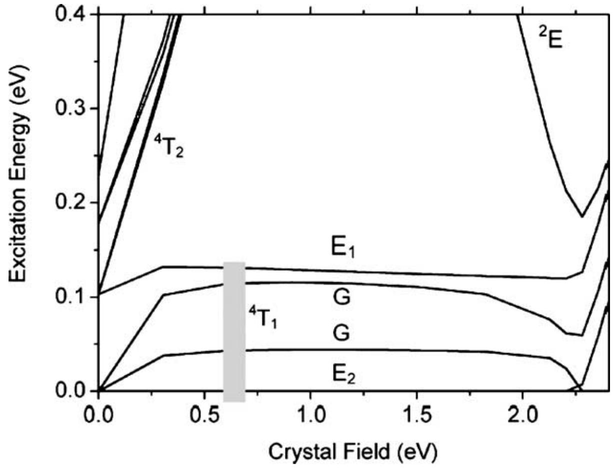

Fig. 6. The Tanabe–Sugano diagram for a $3d^7$ configuration in O_h symmetry. The atomic states of a $3d^7$ configuration are split by electrostatic interactions and within the first 0.4 eV above the ground state only the ^4F states are found, split by the atomic 3d spin–orbit splitting. The horizontal axis gives the crystal field in eV and the ^4F ground state is split into the $^4T_{1g}$ ground sate and the $^4T_{2g}$ and $^4A_{2g}$ excited states that quickly move up in energy with the crystal field. The $^4T_{1g}$ state is split into four sub-states as indicated with the grey block. These sub-states are, respectively, the (double group symmetry [11,12]) E_{2g} ground state, a G_g state, another G_g state and a E_{1g} state. At a crystal field value of 2.25 eV the symmetry changes to low-spin and the G_g states mix with the ^2E_g low-spin G_g state.

Table 8
The matrix elements in SO_3 symmetry needed for the calculation of 2p X-ray absorption

$3d^N \rightarrow 2p^5 3d^{N+1}$ in SO_3 symmetry		
Initial state	Transition	Final state
$\langle \mathbf{0}|\mathbf{0}|\mathbf{0} \rangle$	$\langle \mathbf{0}|\mathbf{1}|\mathbf{1} \rangle$	$\langle 0|0|0 \rangle$
$\langle 1|0|1 \rangle$	$\langle 1|1|0 \rangle$ $\langle 1|1|1 \rangle$ $\langle 1|1|2 \rangle$	$\langle \mathbf{1}|\mathbf{0}|\mathbf{1} \rangle$
$\langle 2|0|2 \rangle$	$\langle 2|1|1 \rangle$ $\langle 2|1|3 \rangle$	$\langle 2|0|2 \rangle$
$\langle 3|0|3 \rangle$	$\langle 3|1|2 \rangle$ $\langle 3|1|3 \rangle$ $\langle 3|1|4 \rangle$	$\langle 3|0|3 \rangle^*$
$\langle 4|0|4 \rangle^*$	$\langle 4|1|3 \rangle^*$ $\langle 4|1|4 \rangle^*$	$\langle 4|0|4 \rangle^*$

Boldface and * matrix elements apply to, respectively, a $3d^0$ and a $3d^8$ configuration.

low-spin transition at 2.25 eV and also the important effect of the 3d spin–orbit coupling. It can be observed that the atomic multiplet spectrum of Co^{II} has a large number of states at low energy. All these states are part of the $^4F_{9/2}$ configuration that is split by the 3d spin–orbit coupling. After applying a cubic crystal field, most of these multiplet states are shifted to higher energies and only four states remain at low energy. These are the four states of $^4T_{1g}$ as indicated in Table 7. These four states all remain within 0.1 eV from the E_2 ground state. That this description is actually correct was shown in detail for the 2p X-ray absorption spectrum of CoO [12], which has a cubic crystal field of 1.2 eV. At 2.25 eV the high-spin low-spin transition is evident. A new state is coming from high energy and a G-symmetry state replaces the E_2 symmetry state at the lowest energy. In fact there is a very interesting complication: due to the 3d spin–orbit coupling the G-symmetry states of the $^4T_{1g}$ and ^2E_g configurations mix and form linear combinations. Around the transition point, this linear combination will have a spin-state that is neither high-spin nor low-spin and in fact a mixed spin-state can be found.

1.4.6. The effects on the X-ray absorption calculations

Table 8 gives all matrix element calculations that have to be carried out for $3d^N \rightarrow 2p^5 3d^{N+1}$ transitions in SO_3 symmetry for the J-values up to 4.We will use the transitions $3d^0 \rightarrow 2p^5 3d^1$ as examples. $3d^0$ contains only $J = 0$ symmetry states, indicated in boldface. This limits the calculation for the ground state spectrum to only one ground state, one transition and one final state matrix element, given in boldface. In case of $3d^8$ Ni^{II} the ground state has a $^3F_4$ configuration, indicated as underlined. We are now going to apply the $SO_3 \rightarrow O_h$ branching rule to this table. The $J = 4$ ground state has transitions to $J = 3$ and 4 final states (Table 8).

Table 9
The matrix elements in O_h symmetry needed for the calculation of 2p X-ray absorption

$3d^N \rightarrow 2p^5 3d^{N+1}$ in O_h symmetry		
Initial state	Transition	Final state
$\langle \mathbf{A_1}|\mathbf{A_1}|\mathbf{A_1} \rangle$	$\langle \mathbf{A_1}|\mathbf{T_1}|\mathbf{T_1} \rangle$	$\langle A_1|A_1|A_1 \rangle$
$\langle T_1|A_1|T_1 \rangle$	$\langle T_1|T_1|A_1 \rangle$ $\langle T_1|T_1|T_1 \rangle$ $\langle T_1|T_1|E \rangle$ $\langle T_1|T_1|T_2 \rangle$	$\langle \mathbf{T_1}|\mathbf{A_1}|\mathbf{T_1} \rangle^*$
$\langle E|A_1|E \rangle$	$\langle E|T_1|T_1 \rangle$ $\langle E|T_1|T_2 \rangle$	$\langle E|A_1|E \rangle^*$
$\langle T_2|A_1|T_2 \rangle^*$	$\langle T_2|T_1|T_1 \rangle^*$ $\langle T_2|T_1|E \rangle^*$ $\langle T_2|T_1|T_2 \rangle^*$ $\langle T_2|T_1|A_2 \rangle^*$	$\langle T_2|A_1|T_2 \rangle^*$
$\langle A_2|A_1|A_2 \rangle$	$\langle A_2|T_1|T_2 \rangle$	$\langle A_2|A_1|A_2 \rangle^*$

Boldface and * matrix elements apply to, respectively, a $3d^0$ and a $3d^8$ configuration.

In octahedral symmetry one has to calculate five matrices for the initial and final states and thirteen transition matrices. Note that this is a general result for all even numbers of 3d electrons, as there are only these five symmetries in O_h symmetry. In the $3d^0$ case, the ground state branches to A_1 and only three matrices are needed to generate the spectral shape: $\langle A_1|A_1|A_1 \rangle$ for the $3d^0$ ground state, $\langle A_1|T_1|T_1 \rangle$ for the dipole transition and $\langle T_1|A_1|T_1 \rangle$ for the $2p^5 3d^1$ final state (Table 9). The $3d^0$systems are rather special because they are not affected by ground state effects. Table 10 shows that a $2p^5 3d^1$ configuration has twelve representations in SO_3 symmetry that are branched to 25 representations in a cubic field. From these 25 representations, only seven are of interest for the calculation of the X-ray absorption spectral shape, because only these T_1 symmetry states obtain a finite intensity.

In the $3d^8$ case, the ground state branches to T_{2g}, i.e. $^3A_{2g} = T_{1g} \otimes A_{2g} = T_{2g}$. The T_{2g} ground state yields dipole transitions to four different final state symmetries, using $T_{2g} \otimes T_{1u} = T_{1u} + T_{2u} + E_u + A_{2u}$. Consequently the complete spectral shape is given by calculating one ground state

Table 10
The branching of the J-values in SO_3 symmetry to the representations in O_h symmetry, using the degeneracies of the $2p^5 3d^1$ final state in X-ray absorption

J in SO_3	Degree	Branchings	Γ in O_h	Degree
0	1	A_{1u}	$A_{1u[0,4]}$	2
1	3	$3 \times T_{1u}$	$A_{2u[3]}$	3
2	4	$4 \times E_u$, $4 \times T_{2u}$	$T_{1u[1,3,4]}$	7
3	3	$3 \times A_{2u}$, $3 \times T_{1u}$,$3 \times T_{2u}$	$T_{2u[2\text{-}4]}$	8
4	1	A_{1u}, E_u, T_{1u}, T_{2u}	$E_{u[2,4]}$	5
$\sum$	12			25

The symmetry in O_h is given, including the SO_3 origin of the states in square brackets.

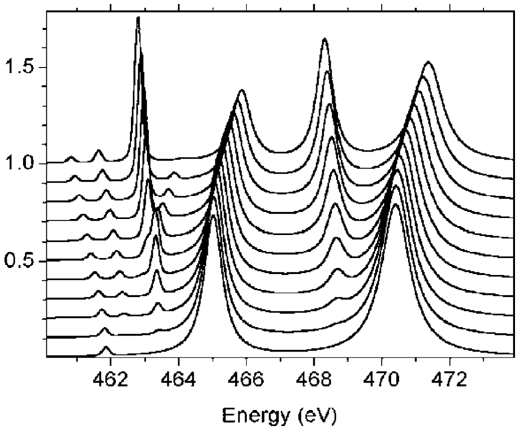

Fig. 7. The crystal field multiplet calculations for the $3d^0 \rightarrow 2p^5 3d^1$ transition in T^{IIV}. The atomic Slater–Condon and spin–orbit coupling parameters were used as given in Table 3. The bottom spectrum is the atomic multiplet spectrum. Each next spectrum has a value of 10Dq that was increased by 0.3 eV. The top spectrum has a crystal field of 3.0 eV.

matrix ($\langle T_{2g}|A_{1g}|T_{2g}\rangle$), four transition matrices and four final state matrices and combining all corresponding matrices to yield the intensities and initial and final state energies. Because the $2p^5 3d^9$ configuration is equivalent to a $2p^5 3d^1$ configuration, the degeneracies of the $2p^5 3d^9$ final state matrices can also be found in Table 10.

Fig. 7 shows the crystal field multiplet calculations for the $3d^0 \rightarrow 2p^5 3d^1$ transition in Ti^{IV}. The result of each calculation is a set of seven energies with seven intensities. These seven states were broadened by the lifetime broadening and the experimental resolution. From a detailed comparison to experiment it turns out that each of the four main lines has to be broadened differently [13–15]. An additional difference in broadening is found between the t_{2g} and the e_g states. This broadening was ascribed to differences in the vibrational effects on the t_{2g}, respectively, the e_g states. Another cause could be a difference in hybridization effects and in fact charge transfer multiplet calculations [16–18] indicate that this effect is more important than vibrational effects.

Fig. 8 compares the crystal field multiplet calculation of the $3d^0 \rightarrow 2p^5 3d^1$ transition in Ti^{IV} with the experimental 2p X-ray absorption spectrum of $FeTiO_3$. The titanium ions are surrounded by six oxygen atoms in a distorted octahedron. The value of 10Dq was set to 1.8 eV. The calculation is able to reproduce all peaks that are experimentally visible. In particular the two small pre-peaks can be nicely observed. The similar spectrum of $SrTiO_3$ has an even sharper spectral shape, related to the perfect octahedral surrounding [19,20].

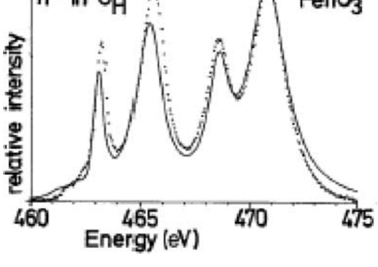

Fig. 8. The 2p X-ray absorption spectrum of $FeTiO_3$ compared with a crystal field multiplet calculation for T^{IIV} with a value of 10Dq of 1.8 eV (reprinted with permission from [14], copyright 1990 American Physical Society).

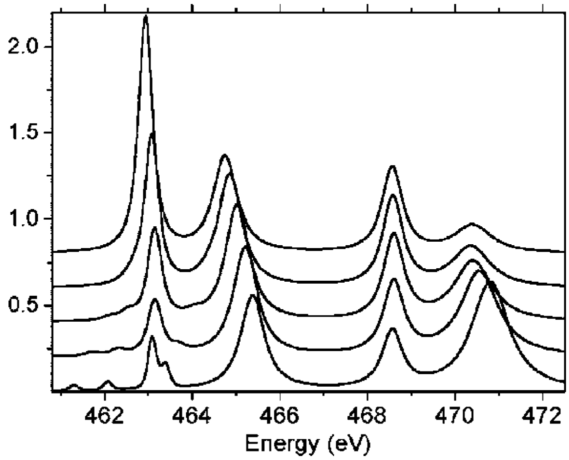

Fig. 9. The crystal field multiplet calculations for the $3d^0 \rightarrow 2p^5 3d^1$ transition in Ti^{IV}. The atomic Slater–Condon and spin–orbit coupling parameters were used as given in Table 3. The bottom spectrum is the crystal field multiplet spectrum with atomic parameters and corresponds to the fifth spectrum in Fig. 8; i.e. 10Dq is 1.5 eV. Each next spectrum has a value of the Slater integrals further reduced by, respectively, 25, 50, 75 and 100%, i.e. the top spectrum is the single particle result.

Fig. 9 shows the effect of the pd Slater–Condon parameters on the spectral shape of the $3d^0 \rightarrow 2p^5 3d^1$ transition in T^{IIV}. The bottom calculation is the same as in Fig. 8 and used the 80% reduction of the Hartree–Fock values in order to obtain a good estimate of the values in the free atom. In most solids the pd Slater–Condon parameters have the same values as for the free atom, in other words, the solid state screening of the pd Slater–Condon parameters is almost zero. The five spectra are calculated by using the same values for the 3d- and 2p-spin–orbit coupling and the same crystal field value of 1.8 eV. The Slater–Condon parameters are rescaled to, respectively, 80% (bottom), 60, 40, 20 and 0% (top). The top spectrum corresponds to the single particle picture, where one expects four peaks, respectively, the L_3–t_{2g}, the L_3–e_g, the L_2–t_{2g} and the L_2–e_g peak, with respective intensities given by their degeneracies, i.e. 6:4:3:2. This is exactly what is observed, where it is noted that the intensity ratio is a little obscured by the differences in line width. One can conclude that there is a large difference between the single particle result (top spectrum) and the multiplet result (bottom spectrum). The Slater–Condon parameters have the effect to lower the intensity of the t_{2g} peaks and shift intensity to the e_g peaks. An even larger intensity shift can be observed from the L_3 edge to the L_2 edge and a very clear effect is the creation of additional (pre-)peaks, because additional transitions become allowed.

Table 11
The branching of the 25 representations in O_h symmetry to 45 representations in D_{4h} symmetry, using the degeneracies of the $2p^53d^1$ final state in X-ray absorption

Γ in O_h	Degree		Γ in D_{4h}		Degree
A_{1u}	2	A_{1u}	A_{1u}	2 + 5	7
A_{2u}	3	B_{1u}	A_{2u}	7	7
T_{1u}	7	$E_u + A_{2u}$	B_{1u}	3 + 5	8
T_{2u}	8	$E_u + B_{2u}$	B_{2u}	8	8
E_u	5	$A_{1u} + B_{1u}$	E_u	7 + 8	15
$\sum$	25				45

More precisely, it is only the L_3 edge that is split and its two states are split in five states. The L_2 edge is not split, and in fact because of this the L_2 edge can be expected to stay closer to the single particle result, in particular the energy separation between the t_{2g} and e_g level of the L_2 edge is only little affected. This is important in those cases where the multiplet effects are smaller, such as for the $L_{2,3}$ edges of the 4d-elements. In the case of 4d-elements, their L_2 edge can be expected to be closer related to the single particle picture than the corresponding L_3 edge.

1.4.7. 3d Systems in lower symmetries

If one reduces the symmetry further from O_h to D_{4h} the seven lines in the X-ray absorption spectrum of Ti^{IV} split further. The respective degeneracies of the representations in O_h symmetry and the corresponding symmetries in D_{4h} symmetry are collected in Table 11.

A $2p^53d^1$ configuration has twelve representations in SO_3 symmetry that are branched to 25 representations in a cubic field. These 25 representations are further branched to 45 representations in D_{4h} symmetry, of the overall degeneracy of 60. From these 45 representations, 22 are of interest for the calculation of the X-ray absorption spectral shape, because they have either E_u or A_{2u} symmetry. There are now two different final state symmetries possible because the dipole operator is split into two representations. The spectrum of two-dimensional E-symmetry relates to the in-plane direction of the tetragon, while the one-dimensional A_{2u}-symmetry relates to the out-of-plane direction.

Examples of this angular dependence in D_{4h} and lower symmetries can be found in the study of interfaces, surfaces and adsorbates. A detailed study of the symmetry effects on the calcium 2p X-ray absorption spectra at the surface and in the bulk of CaF_2 did clearly show the ability of the multiplet calculations to reproduce the spectral shapes both in the bulk as at the reduced C_{3v} symmetry of the surface [21]. Recently, the group of Anders Nilsson performed potassium 2p X-ray absorption experiments of potassium adsorbed on Ni(1 0 0) as well as the co-adsorption system CO/K/Ni(1 0 0) [22]. Fig. 10 shows the K 2p X-ray absorption spectra of K/Ni(1 0 0) compared with CO/K/Ni(1 0 0). The co-adsorption system shows significantly more structural details, which is caused by the strong (crystal) field of the CO molecules on the K ions. The CO and K adsorbates are considered to be placed on, respectively, the black and white squares of a checkers game. Each K ion is surrounded by the four CO molecules in plane as well as the nickel surface below and vacuum above. This C_{4v} symmetry field is expected to have significant angular dependence between the X-ray absorption spectral shape in-plane and out-of-plane. This is shown in the bottom half of Fig. 10. Two asymmetric peaks are visible for (near) grazing incidence and four peaks are visible at normal incidence.

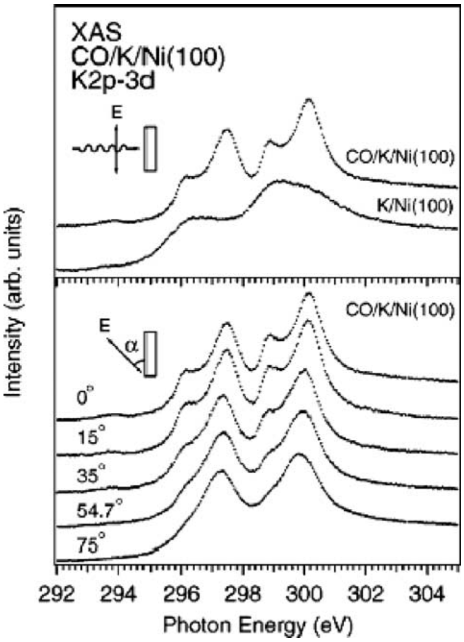

Fig. 10. Upper panel: Potassium 2p3d XAS spectra obtained for K/Ni(1 0 0) and CO/K/Ni(1 0 0), with the E vector parallel to the surface. Lower panel: K 2p3d XAS spectra obtained for CO/K/Ni(1 0 0); the angle α is given as the deviation of the electric field vector from the surface plane (reprinted with permission from [22], copyright 1990 American Physical Society).

Fig. 11 shows a crystal field multiplet calculation of the K 2p X-ray absorption spectrum in C_{4v} symmetry. The calculation reproduces the two asymmetric peaks that are visible for grazing incidence and four peaks at normal incidence. At normal incidence the electric field of the X-ray probes the bonds that are in the direction along the Ni(1 0 0) surface. This are the bonds/interactions between the K ion and the CO molecules. Because of the four CO molecules surrounding the K ion, this interaction induced a clear energy difference between the $3d_{x2-y2}$ orbitals pointing towards the CO molecules and $3d_{xy}$ orbitals pointing in between the CO molecules. It is the energy difference between these orbitals that causes the two peaks to be present. This effect can be nicely shown by using exactly the same crystal field parameters and reducing the Slater–Condon parameters to zero. This single particle limit is shown in the bottom half of Fig. 11.

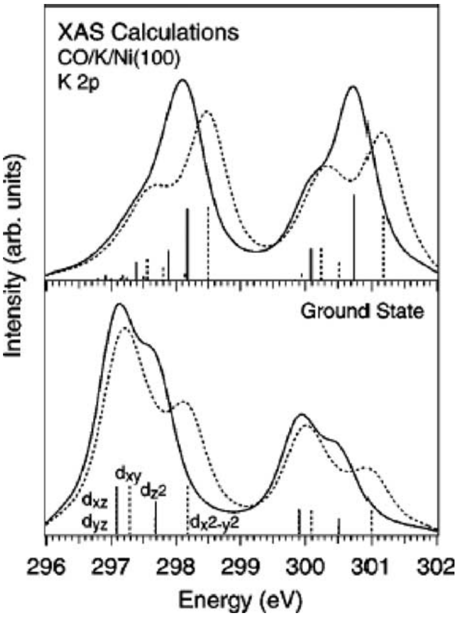

Fig. 11. Crystal field multiplet calculation of a K^I ion in C_{4v} symmetry. The Dq, Ds, and Dt parameters (given in the text) have been optimized to experiment (upper panel). Exactly the same calculation with the 2p3d Slater–Condon parameters set to zero. The four symmetry states are directly visible. The 0° spectra are given with dashed lines and sticks and the 75° spectra with solid lines and sticks (lower panel) (reprinted with permission from [22], copyright 1990 American Physical Society).

1.4.8. X-ray absorption spectra of $3d^N$ systems

The description of the X-ray absorption spectra of systems with a partly filled 3d-band follows the same procedure as for $3d^0$ systems as described above. The matrix elements must be solved for the initial state Hamiltonian, the transition operator and the final state Hamiltonian.

A difference between $3d^0$ and $3d^N$ ground states is that the latter are affected by dd-interactions and crystal field effects. Whether a system is high-spin or low-spin can be determined directly from the shape of the X-ray absorption spectrum. The calculation of the X-ray absorption spectrum has the following parameters to consider.

(a) The atomic Slater–Condon parameters. For trivalent and tetravalent systems these parameters are sometimes reduced. An effective reduction can also (partly) be achieved by the inclusion of charge transfer effects.
(b) The inclusion of the cubic crystal field strength 10Dq, optimized to experiment. The value of 10Dq determines the spin-state of the $3d^4$ to $3d^7$ systems.
(c) The inclusion of the atomic 3d spin–orbit coupling. Because of an effective quenching of the 3d spin–orbit coupling by lower symmetries and/or translational effects, in some cases the 3d spin–orbit coupling must be set to zero to achieve a good agreement with experiment. This is, for example, the case for CrO_2. In contrast the case of CoO proves the importance of the inclusion of the 3d spin–orbit coupling as is evident from Fig. 12.

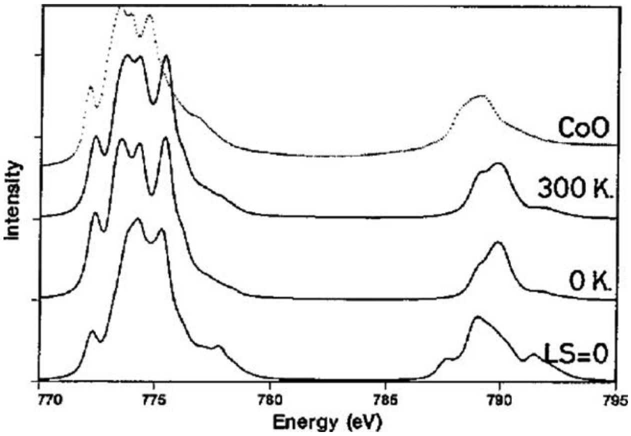

Fig. 12. The crystal field multiplet calculation of Co^{II} with and without the inclusion of the 3d spin–orbit coupling. The bottom spectrum is without 3d spin–orbit coupling. The 0 and 300 K spectra have an atomic spin–orbit coupling included, where the close degeneracy of the spin–orbit split states causes temperature effects in the X-ray absorption spectral shape. The experimental CoO spectrum is simulated with the 300 K spectrum.

(d) The inclusion of lower-symmetry parameters, for example, Ds and Dt.
(e) In many systems it is important to extend the crystal field multiplet program with the inclusion of charge transfer effects as will be discussed in Section 1.5.

1.5. The charge transfer multiplet model

Charge transfer effects are the effects of charge fluctuations in the initial and final states. The atomic multiplet and crystal field multiplet model use a single configuration to describe the ground state and final state. One can combine this configuration with other low-lying configurations similar to the way configuration–interaction works with a combination of Hartree–Fock matrices.

1.5.1. Initial state effects

The charge transfer method is based on the Anderson impurity model and related short-range model Hamiltonians that were applied to core level spectroscopies. This line of approach was developed in the eighties by the groups of Jo and Kotani [23], Gunnarsson and Schönhammer [24], Fujimori and Minami [25] and Sawatzky and co-workers [26–28]. There are variations between the specific methods used, but in this review we sketch only the main line of reasoning behind these models. For details is referred to the original papers.

The Anderson impurity model describes a localized state, the 3d-state, which interacts with delocalized electrons in bands. The Anderson impurity model is usually written in second quantization. In second quantization one starts with the ground state ψ_0 and acts on this state with operators that annihilate ($a^\dagger$) or create (a) a specific electron. For example, a 2p to 3d X-ray absorption transition is writ-

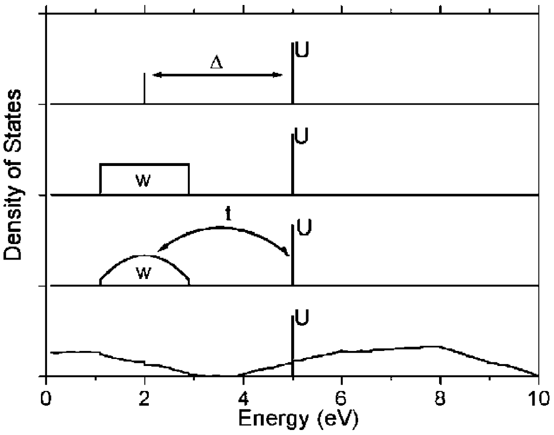

Fig. 13. The interaction of a *U*-correlated localized state with delocalized bands. From bottom to top are, respectively, given: a general DOS, a semi-elliptical valence band, a square valence band and a single valence state.

ten as $|\psi_0 a^{\dagger}_{2p} a_{3d}\rangle$. With second quantization one can also indicate the mixing of configurations in the ground state. For example, an electron can hop from the 3d-states to a state in the (empty) conduction band, i.e. $|\psi_0 a^{\dagger}_{3d} a_{ck}\rangle$, where a_{ck} indicates an electron in the conduction band with reciprocal-space vector *k*. Comparison to experiment has shown that the coupling to the occupied valence band is more important than the coupling to the empty conduction band. In other words, the dominant hopping is from the valence band to the 3d-states. If one annihilates an electron in a state and then re-creates it one effectively is counting the occupation of that state, i.e. $a^{\dagger}_{3d} a_{3d}$ yields n_{3d}. The Anderson impurity Hamiltonian can then be given as:

$$H_{\mathrm{AIM}} = \varepsilon_{3d} a^{\dagger}_{3d} a_{3d} + U_{dd} a^{\dagger}_{3d} a_{3d} a^{\dagger}_{3d} a_{3d} + \sum_{k} \varepsilon_{vk} a^{\dagger}_{vk} a_{vk} + t_{v3d} \sum_{k} (a^{\dagger}_{3d} a_{vk} + a^{\dagger}_{vk} a_{3d})$$

These four terms represent, respectively, the 3d-state, the correlation of the 3d-state, the valence band and the coupling of the 3d-states with the valence band. One can further extend the Anderson Impurity model to include more than a single impurity, i.e. impurity bands. In addition, one can include correlation in the valence band, use larger clusters, etc. In case of multiplet calculations of X-ray absorption these approaches lead in most cases to a too large calculation. There has been much work for the $\mathrm{Cu^{II}}$ case, in particular in connection to the high Tc superconductors [29], and also there have been calculations concerning the effects of non-local screening on larger clusters for $\mathrm{Ni^{II}}$ [30].

Fig. 13 sketches the Impurity model with a semi-elliptical band of bandwidth *w*. Instead of a semi-elliptical band one can use the actual band structure that is found from DFT calculations (bottom). It has been demonstrated that the use of the real band structure instead of an approximate semi-elliptical or square band structure hardly affects the spectral shape [31]. The multiplet model approximates the band usually as a square of bandwidth *w*, where *n* number of points of equal intensity are used for the actual calculation. Often one simplifies the calculation further to $n = 1$, i.e. a single state representing the band. In that case the bandwidth is reduced to zero. In order to simplify the notation we will in the following remove the *k*-dependence of the valence band and assume a single state describing the band. It must be remembered however that in all cases one can change back this single state to a real band with bandwidth *w*.

Removing the *k*-dependence renders the Hamiltonian into:

$$H_{\mathrm{AIM-1}} = \varepsilon_{3d} a^{\dagger}_{3d} a_{3d} + U_{dd} a^{\dagger}_{3d} a_{3d} a^{\dagger}_{3d} a_{3d} + \varepsilon_{k} a^{\dagger}_{v} a_{v} + t_{v3d} (a^{\dagger}_{3d} a_{v} + a^{\dagger}_{v} a_{3d})$$

Bringing the multiplet description into this Hamiltonian implies that the single 3d state is replaced by all states that are part of the crystal field multiplet Hamiltonian of that particular configuration. This implies that the U_{dd}-term is replaced by a summation over four 3d-wavefunctions $3d_1$, $3d_2$, $3d_3$ and $3d_4$:

$$H_{\mathrm{AIM}} = \varepsilon_{3d} a^{\dagger}_{3d} a_{3d} + \varepsilon_{k} a^{\dagger}_{v} a_{v} + t_{v3d} (a^{\dagger}_{3d} a_{v} + a^{\dagger}_{v} a_{3d}) + \sum_{\Gamma_1,\Gamma_2,\Gamma_3,\Gamma_4} g_{dd} a^{\dagger}_{3d1} a_{3d2} a^{\dagger}_{3d3} a_{3d4} + \sum_{\Gamma_1,\Gamma_2} l \cdot s a^{\dagger}_{3d1} a_{3d2} + H_{\mathrm{CF}}$$

The term g_{dd} describes all two-electron integrals and includes the Hubbard *U* as well as the effects of the Slater–Condon parameters F^2 and F^4. In addition, there is a new term in the Hamiltonian due to the 3d spin–orbit coupling. H_{CF} describes the effects of the crystal field potential Φ. This situation can be viewed as a multiplet of localized states interacting with the delocalized density of states. One ingredient is still missing from this description that is if the electron is transferred from the valence band to the 3d-band, the occupation of the 3d-band changes by one. This $3d^{N+1}$ configuration is again affected by multiplet effects, exactly like the original $3d^{N}$ configuration. The $3d^{N+1}$ configuration contains a valence band with a hole. Because the model is used mainly for transition metal compounds, the valence band is in general dominated by ligand character, for example, the oxygen 2p valence band in case of transition metal oxides. Therefore the hole is considered to be on the ligand and is indicated with $\underline{\mathrm{L}}$, i.e. a ligand hole. The charge transfer effect on the wave function is described as $3d^{N} + 3d^{N+1}\underline{\mathrm{L}}$. If one includes the effects of the multiplets on the $3d^{N+1}\underline{\mathrm{L}}$, a configuration–interaction picture is obtained coupling the two sets of multiplet states.

Fig. 14 gives the crystal field multiplets for the $3d^7$ and $3d^8\underline{\mathrm{L}}$ configurations of $\mathrm{Co^{II}}$. The $3d^7$ configurations is centered at 0.0 eV and the lowest energy state is the $^4T_{1g}$ state, where the small splittings due to the 3d spin–orbit coupling were neglected. The lowest state of the $3d^8\underline{\mathrm{L}}$ configuration is the $^3A_{2g}$ state, which is the ground state of $3d^8$. The cen-

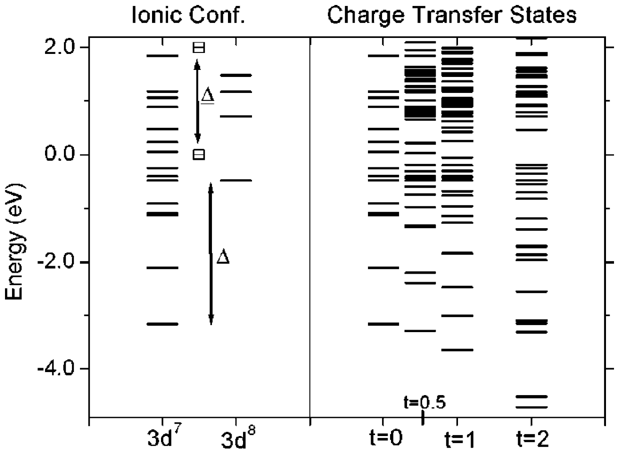

Fig. 14. Left: The crystal field multiplet states of $3d^7$ and $3d^8$ configurations. The multiplet states with energies higher than +2.0 eV are not shown. Δ was set to +2.0 eV. Right: the charge transfer multiplet calculations for the combination of crystal field multiplets as indicated on the left and with the hopping ranging from 0.0 to 2.0 eV as indicated below the states.

ter of gravity of the $3d^8$ configuration was set at 2.0 eV, which identifies with a value of Δ of 2.0 eV. The effective charge transfer energy Δ is defined as the energy difference between the lowest states of the $3d^7$ and the $3d^8\underline{L}$ configurations as indicated in Fig. 14. Because the multiplet splitting is larger for $3d^7$ than for $3d^8\underline{L}$, the effective Δ is larger than Δ. The effect of charge transfer is to form a ground state that is a combination of $3d^7$ and $3d^8\underline{L}$. The energies of these states were calculated on the right half of the figure. If the hopping parameter t is set equal to zero, both configurations do not mix and the states of the mixed configuration are exactly equal to $3d^7$, and at higher energy to $3d^8\underline{L}$. Turning on the hopping parameter, one observes that the energy of the lowest configuration is further lowered. This state will still be the $^4T_{1g}$ configuration, but with increasing hopping, it will have increasing $3d^8\underline{L}$ character. One can observe that the second lowest state is split by the hopping and the most bonding combination obtains an energy that comes close to the $^4T_{1g}$ ground state. This excited state is a doublet state and if the energy of this state would cross with the $^4T_{1g}$ state one would observe a charge-transfer induced spin-transition. It was shown that charge transfer effects can lead to new types of ground states, for example, in case of a $3d^6$ configuration, crystal field effects lead to a transition of a S = 2 high-spin to a S = 0 low-spin ground state. Charge transfer effects are also able to lead to an S = 1 intermediate spin ground state [32].

Fig. 14 can be expanded to Tanabe–Sugano like diagrams for two configurations $3d^N + 3d^{N+1}\underline{L}$, instead of the usual Tanabe–Sugano diagrams as a function of only one configuration. The energies of such two-configuration Tanabe–Sugano diagrams are affected by the Slater–Condon parameters (often approximated with the B Racah parameter), the cubic crystal field 10Dq, the charge transfer energy Δ and the hopping strength t. The hopping can be made symmetry dependent and one can add crystal field parameters related to lower symmetries, yielding to an endless series of Tanabe–Sugano diagrams. What is actually important is to determine the possible types of ground states for a particular ion, say Co^{II}. Scanning through the parameter space of F^2, F^4, 10Dq, Ds, Dt, LS_{3d}, t_Γ and Δ one can determine the nature of the ground state. This ground state can then be checked with 2p X-ray absorption. After the inclusion of exchange and magnetic fields one has also a means to compare the ground state with techniques like X-ray MCD, optical MCD and EPR.

Comparing Fig. 13 with Fig. 14 one observes the transition from a single particle picture to a multiplet configurational picture. One can in principle put more band character into this configurational picture and a first step is to make a transition from a single state to a series of $3d^8\underline{L}$ states, each with its included multiplet but with each a different effective charge transfer energy. One can choose to use a more elaborate cluster model in which the neighbor atoms are actually included in the calculation [29,30,33]. These cluster models are not described further here.

1.5.2. Final state effects

The final state Hamiltonian of X-ray absorption includes the core hole plus an extra electron in the valence region. One adds the energy and occupation of the 2p core hole to the Hamiltonian. The core hole potential U_{pd} and its higher order terms g_{pd} give rise to the overlap of a 2p wave function with a 3d wave function and is given as a summation over two 2p and two 3d-wavefunctions $2p_1$, $2p_2$, $3d_1$ and $3d_2$:

$$H_{2p} = \varepsilon_{2p} a^{\dagger}_{2p} a_{2p} + \sum_{\Gamma_1,\Gamma_2,\Gamma_3,\Gamma_4} g_{pd} a^{\dagger}_{3d1} a_{2p1} a^{\dagger}_{2p2} a_{3d2} + \sum_{\Gamma_1,\Gamma_2} l\cdot s a^{\dagger}_{2p1} a_{2p2}$$

The term g_{pd} describes all two-electron integrals and includes U_{pd} as well as the effects of the Slater–Condon parameters F^2, G^1 and G^3. In addition, there is a term in the Hamiltonian due to the 2p spin–orbit coupling. There is no crystal field effect on core states.

$$\begin{aligned} H_{AIM} = {} & \varepsilon_{3d} a^{\dagger}_{3d} a_{3d} + \varepsilon_k a^{\dagger}_{v} a_{v} + t_{v3d}(a^{\dagger}_{3d} a_{v} + a^{\dagger}_{v} a_{3d}) \\ & + \sum_{\Gamma_1,\Gamma_2,\Gamma_3,\Gamma_4} g_{dd} a^{\dagger}_{3d1} a_{3d2} a^{\dagger}_{3d3} a_{3d4} \\ & + \sum_{\Gamma_1,\Gamma_2} l\cdot s a^{\dagger}_{3d1} a_{3d2} + H_{CF} + \varepsilon_{2p} a^{\dagger}_{2p} a_{2p} \\ & + \sum_{\Gamma_1,\Gamma_2,\Gamma_3,\Gamma_4} g_{pd} a^{\dagger}_{3d1} a_{2p1} a^{\dagger}_{2p2} a_{3d2} \\ & + \sum_{\Gamma_1,\Gamma_2} l\cdot s a^{\dagger}_{2p1} a_{2p2} \end{aligned}$$

The overall Hamiltonian in the final state is given. This equation is solved in the same manner as the initial state

Hamiltonian. Using the two configuration description of Fig. 14, one finds for $\mathrm{Co}^{\mathrm{II}}$ two final states $2\mathrm{p}^5 3\mathrm{d}^8$ and $2\mathrm{p}^5 3\mathrm{d}^9\underline{\mathrm{L}}$. These states mix in a manner similar to the two configurations in the ground state and as such give rise to a final state Tanabe–Sugano diagram. All final state energies are calculated from the mixing of the two configurations. This calculation is only possible if all final state parameters are known. The following rules are used.

(a) The 2p3d Slater–Condon parameters are taken from an atomic calculation. For trivalent ions and higher valences, these atomic values are sometimes reduced.
(b) The 2p and 3d spin–orbit coupling are taken from an atomic calculation.
(c) The crystal field values are assumed to be the same as in the ground state.
(d) The energies of the configurations, i.e. the charge transfer energy, are given by the values of U_{dd} and U_{pd}. Effectively $\Delta_{\mathrm{F}} = \Delta_{\mathrm{I}} + U_{\mathrm{dd}} - U_{\mathrm{pd}}$. Because in general U_{pd} is approximately 1–2 eV larger than U_{dd}, one often assumes $\Delta_{\mathrm{F}} = \Delta_{\mathrm{I}} - 1$ or -2 eV.
(e) The hopping parameter t is assumed to be equal in the initial and final states.

Detailed analysis of X-ray absorption and resonant X-ray emission spectra has shown that the crystal field values are smaller by 10–20% in the final state [34]. The same observation has been made for the hopping parameters [35]. One can understand these trends from the (slight) compression of the 3d wave function in the final state. From the presence of the 2p core hole one would expect a significant compression of the 3d wave function, but the effect of the 2p core hole is counteracted by the effect of the extra 3d-electron in the final state. Because we have seen that U_{dd} is a bit smaller than U_{pd} this counteracting action is not complete and there will be a small compression of the 3d wave function. In conclusion it can be said that Δ, t and 10Dq will all be slightly smaller in the final state. Because the reduction of these parameters has counteracting effects on the spectral shape, in most simulations one varies only Δ and keeps $\boldsymbol{t}$ and 10Dq constant.

1.5.3. The X-ray absorption spectrum with charge transfer effects

The essence of the charge transfer model is the use of two or more configurations. Ligand field multiplet calculations use one configuration for which it solves the effective atomic Hamiltonian plus the ligand field Hamiltonian, so the following matrices:

$$I_{\mathrm{XAS},1} \propto \langle 3\mathrm{d}^N | \mathrm{p} | 2\mathrm{p}^5 3\mathrm{d}^{N+1} \rangle^2$$

$$H_{\mathrm{INIT},1} = \left\langle 3\mathrm{d}^N \left| \frac{e^2}{r_{12}} + \varsigma_{\mathrm{d}} l_{\mathrm{d}} \cdot s_{\mathrm{d}} + H_{\mathrm{LFM}} \right| 3\mathrm{d}^N \right\rangle$$

$$H_{\mathrm{FINAL},1} = \left\langle 2\mathrm{p}^5 3\mathrm{d}^{N+1} \left| \frac{e^2}{r_{12}} + \varsigma_{\mathrm{p}} l_{\mathrm{p}} \cdot s_{\mathrm{p}} + \varsigma_{\mathrm{d}} l_{\mathrm{d}} \cdot s_{\mathrm{d}} + H_{\mathrm{LFM}} \right| \times 2\mathrm{p}^5 3\mathrm{d}^{N+1} \right\rangle$$

The charge transfer model adds a configuration $3\mathrm{d}^{N+1}\underline{\mathrm{L}}$ to the $3\mathrm{d}^N$ ground state. In case of a transition metal oxide, in a $3\mathrm{d}^{N+1}\underline{\mathrm{L}}$ configuration an electron has been moved from the oxygen 2p-valence band to the metal 3d-band. One can continue with this procedure and add $3\mathrm{d}^{N+2}\underline{\mathrm{L}}^2$ configuration, etc. In many cases two configurations will be enough to explain the spectral shapes, but in particular for high valence states it can be important to include more configurations [36,37]. As far as X-ray absorption and X-ray emission is concerned, the consequences for the calculations are the replacement of $3\mathrm{d}^N$ with $3\mathrm{d}^N + 3\mathrm{d}^{N+1}\underline{\mathrm{L}}$ plus the corresponding changes in the final state. This adds a second initial state, final state and dipole transition:

$$I_{\mathrm{XAS},2} \propto \langle 3\mathrm{d}^{N+1}\underline{\mathrm{L}} | \mathrm{p} | 2\mathrm{p}^5 3\mathrm{d}^{N+2}\underline{\mathrm{L}} \rangle^2$$

$$H_{\mathrm{INIT},2} = \left\langle 3\mathrm{d}^{N+1}\underline{\mathrm{L}} \left| \frac{e^2}{r_{12}} + \varsigma_{\mathrm{d}} l_{\mathrm{d}} s_{\mathrm{d}} + H_{\mathrm{LFM}} \right| 3\mathrm{d}^{N+1}\underline{\mathrm{L}} \right\rangle$$

$$H_{\mathrm{FINAL},2} = \left\langle 2\mathrm{p}^5 3\mathrm{d}^{N+2}\underline{\mathrm{L}} \left| \frac{e^2}{r_{12}} + \varsigma_{\mathrm{p}} l_{\mathrm{p}} s_{\mathrm{p}} + \varsigma_{\mathrm{d}} l_{\mathrm{d}} s_{\mathrm{d}} + H_{\mathrm{LFM}} \right| \times 2\mathrm{p}^5 3\mathrm{d}^{N+2}\underline{\mathrm{L}} \right\rangle$$

The two initial states and two final states are coupled by monopole transitions, i.e. configuration interaction. The mixing parameter $\boldsymbol{t}$ couples both configurations and Δ is the energy difference. The Hamiltonian is abbreviated with $\boldsymbol{t}/\Delta$ to describe the monopole interaction:

$$H_{\mathrm{MIX}\,I1,I2} = \left\langle 3\mathrm{d}^N \left| \frac{t}{\Delta} \right| 3\mathrm{d}^{N+1}\underline{\mathrm{L}} \right\rangle$$

$$H_{\mathrm{MIX}\,F1,F2} = \left\langle 2\mathrm{p}^5 3\mathrm{d}^{N+1} \left| \frac{t}{\Delta} \right| 2\mathrm{p}^5 3\mathrm{d}^{N+2}\underline{\mathrm{L}} \right\rangle$$

The X-ray absorption spectrum is calculated by solving the equations given above. If a $3\mathrm{d}^{N+2}\underline{\mathrm{LL}'}$ configuration is included its energy is $2\Delta + U_{\mathrm{dd}}$, where U_{dd} is the correlation energy between two 3d-electrons [28]. The formal definition of U_{dd} is the energy difference one obtains when an electron is transferred from one metal site to another, i.e. a transition $3\mathrm{d}^N + 3\mathrm{d}^N \rightarrow 3\mathrm{d}^{N+1} + 3\mathrm{d}^{N-1}$. The number of interactions of two $3\mathrm{d}^N$ configurations is one more than the number of interactions of $3\mathrm{d}^{N+1}$ plus $3\mathrm{d}^{N-1}$, implying that this energy difference is equal to the correlation energy between two 3d-electrons.

By analyzing the effects of charge transfer it is found that, for systems with a positive value of Δ, the main effects on the X-ray absorption spectral shape are:

(1) the formation of small satellites; and
(2) the contraction of the multiplet structures.

The formation of small satellites or even the absence of visible satellite structures is a special feature of X-ray absorption spectroscopy. Its origin is the fact that X-ray absorption is a neutral spectroscopy and the local charge of the final state is equal to the charge of the initial state. This implies that there is little screening hence little charge transfer satellites. This effect can be explained by using a two-by-two problem as example. We follow the papers of Hu et al. [9,10] to describe the mixing of two configurations that are separated by Δ and mixed by t. This mixing yields a two by two determinant:

$$H = \begin{vmatrix} 0 & t \\ t & \Delta \end{vmatrix}$$

Solving the determinant yields the two states after mixing: The ground state, or bonding combination, Ψ_B has a wave function:

$$\Psi_\mathrm{B} = \alpha_i|3\mathrm{d}^N\rangle + \beta_i|3\mathrm{d}^{N+1}\mathrm{L}\rangle$$

The energy of the bonding combination is given as:

$$E_\mathrm{B} = \tfrac{1}{2}\Delta - \tfrac{1}{2}\sqrt{\Delta^2 + 4t}$$

The parameters α_i and β_i can be defined in Δ and t:

$$\alpha_i = \sqrt{\frac{1}{1 + (X - \Delta/2T)^2}}, \qquad X = \sqrt{\Delta^2 + 4T^2},$$

$$\beta_i = \sqrt{1 - \alpha_i^2}$$

The anti-bonding combination is given as:

$$\Psi_\mathrm{B} = \beta_i|3\mathrm{d}^N\rangle - \alpha_i|3\mathrm{d}^{N+1}\mathrm{L}\rangle$$

The energy of the anti-bonding combination is given as:

$$E_\mathrm{B} = \tfrac{1}{2}\Delta + \tfrac{1}{2}\sqrt{\Delta^2 + 4t}$$

It can be found that, apart from numerical deviations at small charge transfer energies, the value of α_i is proportional to $\sqrt{\Delta/t}$. The dependence on Δ and t is given in Fig. 15. A linear dependence of α_i is observed as a function of t and a square root dependence is found as a function of Δ. This implies for the percentage of $3\mathrm{d}^N$ character in the ground state, i.e. α_i^2 that it is proportional to Δ/t^2.

We have found that in the final state the value of $\Delta_F \sim \Delta - 1\,\mathrm{eV}$. This implies that the final state determinant is approximately equal to the initial state determinant:

$$H = \begin{vmatrix} 0 & t_F \\ t_F & \Delta_F \end{vmatrix}$$

This yields for α_f and β_f that they are approximately equal to α_i and β_i. The results of the initial and final state equations can be used to calculate the X-ray absorption cross-section. One can make a transition from $3\mathrm{d}^N$ to $2\mathrm{p}^5 3\mathrm{d}^{N+1}$ and from $3\mathrm{d}^{N+1}\mathrm{L}$ to $2\mathrm{p}^5 3\mathrm{d}^{N+2}\mathrm{L}$. This implies that the intensity of the main peak is equal to $(\alpha_i\alpha_\mathrm{f} + \beta_i\beta_\mathrm{f})^2$ while the satellite intensity is equal to $(\alpha_i\beta_\mathrm{f} - \beta_i\alpha_\mathrm{f})^2$. The contraction of the multiplet structure due to charge transfer can also be understood using the two by two matrices. Assume two multiplet states split by an energy δ. They both mix with a charge transfer state that is positioned Δ above the lowest energy multiplet state I. Consequently the charge transfer energy of the second multiplet state II is $\Delta - \delta$. Assuming that the hopping terms are the same for these two states, the energy gain of the bonding combination is:

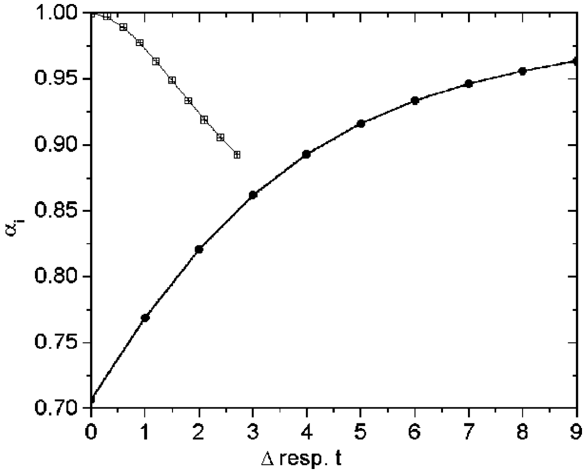

Fig. 15. The initial state value of α as a function of the charge transfer energy Δ for $t = 2.7\,\mathrm{eV}$ (solid circles) and as a function of the hopping t for $\Delta = 5\,\mathrm{eV}$ (open squares).

$$E_\mathrm{B}(\mathrm{I}) = \tfrac{1}{2}\Delta - \tfrac{1}{2}\sqrt{\Delta^2 + 4t}$$

$$E_\mathrm{B}(\mathrm{II}) = \tfrac{1}{2}\Delta - \delta - \tfrac{1}{2}\sqrt{(\Delta - \delta)^2 + 4t}$$

These trends are made visible in Fig. 16. One can observe that for zero hopping there is no energy gain. Consider, for example, a hopping of 1.5 eV. Then one observes the largest energy gain for the lowest value of Δ. The higher lying

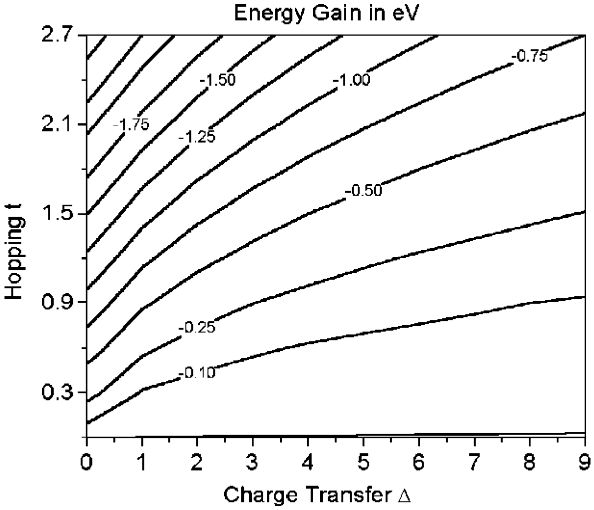

Fig. 16. The energy gain of the bonding combination of a two-state problem as a function of the charge transfer energy Δ and the hopping t.

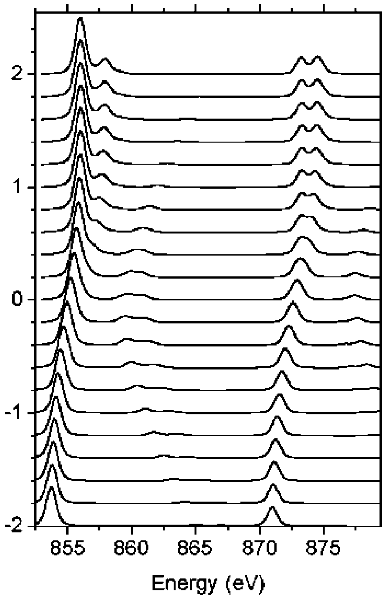

Fig. 17. Series of charge transfer multiplet calculations for the Ni$^{\mathrm{II}}$ ground state $|3d^8 + 3d^9\underline{L}>$. The top spectrum has a charge transfer energy of +10 eV. The bottom spectrum has a charge transfer energy of −10 eV and relates to an almost pure 3d^9 ground state.

multiplet states have a smaller effective Δ and consequently a larger energy gain. As such their energy comes closer to the lowest energy state and the multiplet appears compressed.

The two by two problem in the initial and final state explains the two main effects of charge transfer: a compression of the multiplet structure and the existence of only small satellites. These two phenomena are visible in Fig. 17. In case that the charge transfer is negative, the satellite structures are slightly larger because then the final state charge transfer is increased with respect to the initial state and the balance of the initial and final state α's and β's is less good.

Fig. 17 shows the effect of the charge transfer energy on divalent nickel. We have used the same hopping t for the initial and final state and reduced the charge transfer energy Δ by 1 eV. In the top spectrum, $\Delta = 10$ and the spectrum is the ligand field multiplet spectrum of a Ni$^{\mathrm{II}}$ ion in its 3d^8 configuration. The bottom spectrum uses $\Delta = -10$ and now the ground state is almost a pure $3d^9\underline{L}$ configuration. Looking for the trends in Fig. 17, one finds the increased contraction of the multiplet structure by going to lower values of Δ. This is exactly what is observed in the series NiF_2 to $NiCl_2$ and $NiBr_2$ [16,17,27,38]. Going from Ni to Cu the atomic parameters change little, except the 2p spin–orbit coupling and the 2p binding energy. Therefore the spectra of 3d^N systems of different elements are all similar and the bottom spectrum is also similar to Cu$^{\mathrm{II}}$ systems. Therefore one can also use the spectra with negative Δ-values for Cu$^{\mathrm{III}}$ compounds, such as $La_2Li_{1/2}Cu_{1/2}O_4$ and Cs_2KCuF_6. Fig. 18 shows the comparison of the 2p X-ray absorption spectrum of these two compounds with charge transfer multiplet calculations [39,40]. It can be checked in Fig. 17 that these calculations look similar to the calculations for Ni$^{\mathrm{II}}$ systems with negative values of Δ. For such systems with negative Δ values, it is important to carry out charge transfer multiplet calculations, as no good comparison with crystal field multiplet spectra can be made.

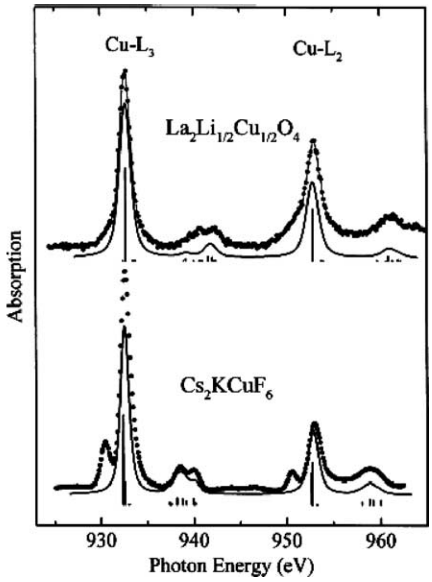

Fig. 18. Results of theoretical simulations of the copper 2p X-ray absorption spectra of Cs_2KCuF_6 (bottom) and $La_2Li_{1/2}Cu_{1/2}O_4$ (top), in comparison with the experimental spectra (reprinted with permission from [38], copyright 1998 Elsevier Science).

2. An overview of X-ray spectroscopies

In this section we use the solid NiO as an example to introduce the range of different X-ray spectroscopies. It should be noted that we limit ourselves to the ‘multiplet aspects’ of the various spectroscopies. A complete discussion of the spectroscopies is outside the scope of this review.

The ground state of NiO in the charge transfer multiplet model will be described as $3d^8{+}3d^9\underline{L}$. We will use this ground state to describe a number of X-ray spectroscopies. In the ground state, the atomic Slater–Condon parameters are used. These values are determined by Hartree–Fock calculations scaled to 80% of their value. Also the atomic spin–orbit coupling of 0.08 eV is used. The ionic crystal field value is set to 0.7 eV and the hopping parameters are set to 2.2 eV for e_g hopping and 1.1 eV for t_{2g} hopping. The charge transfer energy Δ is set to 3.0 eV. These parameters yield a ground state of $^3A_{2g}$ symmetry that is build from 82% 3d^8 character and 18% $3d^9\underline{L}$ character. Inclusion of $3d^{10}\underline{LL}'$ adds only a 0.5% contribution to the ground state and will be neglected.

2.1. X-ray absorption (XAS)

Fig. 19 gives the 2p X-ray absorption that has been described in detail in Section 1. The dipole transition trans-

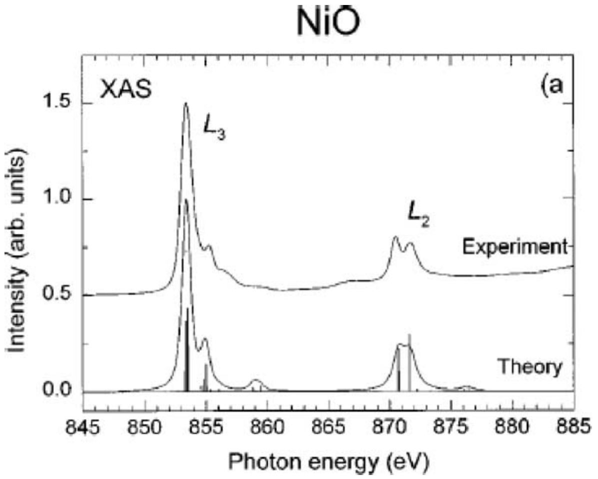

Fig. 19. 2p X-ray absorption spectrum of NiO (top) compared with a charge transfer multiplet calculation (bottom) as described in the text (reprinted with permission from [41], copyright 1999 American Physical Society).

forms the $3d^8$+$3d^9L$ ground state to $2p^53d^9$+$2p^53d^{10}L$. The final state charge transfer is reduced from 3.5 to 2.0 eV due to the slightly larger pd exchange with respect to the dd-exchange. In some calculations the hopping terms were also reduced from 2.2 to 1.8 eV [41].

The 1s X-ray absorption spectrum of NiO is given by single particle models and will not be discussed in detail here. The pre-edge structure of the 1s XAS spectrum is important as it is used for resonance studies. In addition, the pre-edge is determined by quadrupole transitions directly into the 3d-band and as such the final state is affected by the 3d3d correlation effects. NiO is a bit special in this respect, as the quadrupole transition will give a final state $1s^13d^9$+$1s^13d^{10}L$. The mixing in this final state is similar as in the initial state, i.e. Δ/t^2 is approximately constant. In addition, there are effectively no multiplet effects and the ground state is rather pure in $3d^8$ character (80%), which implies that the influence of the ligand hole state on the pre-edge calculation is negligibly small. The final state can be approximated with a $1s^13d^9$ state and with absence of multiplet effects and dd-correlation (as there is only one 3d-hole left), this final state relates to a single line.

The 3p X-ray absorption spectrum has a similar description as the 2p X-ray absorption spectrum. The final state relates to the states $3p^53d^9 + 3p^53d^{10}L$ and the experimental spectrum is simulated well. Some additional effects are important, in particular the lifetime broadening of the $3p^53d^9$ varies with excitation energies [42]. In addition, there is a dominant transition in the spectral shape at the high energy side of the spectral shape. This is the so-called delayed onset, which is a feature that occurs due to multiplet effects, in particular the small core hole spin–orbit coupling and large exchange interactions that cause the final state to be close to its LS-symmetry limit.

2.2. X-ray photoemission (XPS)

X-ray photoemission (XPS) describes exactly the same process as X-ray absorption, i.e. the excitation of a core electron from the ground state to some excited state. A difference with X-ray absorption is the difference in measurement. XAS measures the variation in the absorption with respect to the excitation energy, while XPS measures the variation in the kinetic energy of the emitted electron at a constant excitation energy. This immediately gives rise to the observation that one can combine XAS and XPS and measure the XPS spectra as a function of the X-ray excitation energy, for example, while scanning through an absorption edge.

2p XPS spectra can be calculated with the same charge transfer multiplet model as 2p XAS spectra. The $3d^8$+$3d^9L$ ground state is excited to $2p^53d^9$+$2p^53d^{10}L$ in 2p XAS and to $2p^53d^8\varepsilon_s + 2p^53d^9L\varepsilon_s$, where ε_s is a free electron of s-character. A free electron is within the charge transfer multiplet model defined as an electron without correlation effects. Instead of an ϵ_s electron, also excitations to a d-electron (ε_d) are calculated. The fact that in 2p XAS the electron is excited to a 3d-state implies that the 2p XAS process is self-screened. In contrast, the 2p XPS process is an ionizing effect that caused large screening effects. Table 12 gives the relative energies of the two configurations in the various XAS and XPS experiments. It can be seen that the 2p XPS final state contains a real charge transfer effect, in the sense that the state with the lowest energy has a different number of 3d-electrons in the final state with respect to the initial state. This implies large charge transfer satellites as can be seen in the calculation of the 2p XPS spectrum of NiO. In case of 2p XPS it becomes important to include a third configuration $3d^{10}\underline{LL}'$ to the ground state because

Table 12
The configurations and energies of the ground state and the final states in 2p XAS, 2p XPS, 1s XAS and 1s XPS

	Configurations	Energy	Remarks
Ground state	$3d^8$+$3d^9L$	$\Delta = 3.0$	
2p XAS	$2p^53d^9$+$2p^53d^{10}L$	$\Delta + U - Q_{2p} = 2.0$	
1s XAS	$1s^13d^9$+$1s^13d^{10}L$	$\Delta + U - Q_{1s} = 1.5$	Pre-edge
	$1s^13d^84p^1$+$1s^13d^9L4p^1$	$\Delta - Q_{1s} + U_{4p} = -4.5$	Edge
2p XPS	$2p^53d^8\varepsilon$+$2p^53d^9L\varepsilon$	$\Delta - Q_{2p} = -5.0$	
1s XPS	$1s^13d^8\varepsilon$+$1s^13d^9L\varepsilon$	$\Delta - Q_{1s} = -5.5$	

in the final state it is lowered in energy and mixes with the $3d^8$ and $3d^9$ final states. 3s and 3p XPS follow the same energy scheme as 2p XPS. The multiplet effects of a 3p and a 3s core hole are different causing a different spectral shape [38,40,41].

2.3. Resonant photoemission and Auger

In case of XPS one can choose the excitation energy of the X-ray excitation. For example, one can measure the 3p XPS spectrum of NiO at all energies above the binding energy of the 3p core state. The choice of the X-ray energy in turn implies that one varies the kinetic energy of the excited core electron. The combination of X-ray excitation energy and electron kinetic energy can be used to vary the penetration/escape depth of the experiment and as such to change the effective probing depth from a few nanometers to micrometers.

If a core hole is created it will decay on a femto second timescale. For shallow core holes, the dominant decay process is the so-called Auger process. In an Auger process the core hole is filled by a shallow core electron while at the same time another core electron is excited. For example, a 3p core electron fills a 2p core hole, while a second 3p core electron is excited. The kinetic energy of the excited electron is given by the difference in binding energy between a 2p core hole and two 3p core holes (including all correlation effects). The Auger matrix elements are two-electron interaction matrices, equivalent to the two-electron matrices that give rise to multiplet effects. For example, a 2p3d multiplet interaction can be written as $\langle 2p3d|1/r|2p3d\rangle$ and similarly a 2p3p3p Auger decay can be written as $\langle 2p3p|1/r|3p\varepsilon_p\rangle$, etc. Usually Auger transitions are given as KLL Auger for the 1s2p2p decay channel, etc. Table 13 gives the Auger decay channels involving all combinations of 3s, 3p and valence band 3d core holes after exciting a 2p core hole, either on resonance in 2pXAS or off-resonance with 2p XPS.

2.3.1. Resonant photoemission

Resonant photoemission is the experiment in which one, for example, can scan through a 2p XAS spectrum and measures at every excitation energy the 3p XPS spectral shape. Off resonance, the 3p XPS spectral shape is given by the transition from the $3d^8+3d^9\underline{L}$ ground state to the $3p^5 3d^8\varepsilon + 3p^5 3d^9\underline{L}\varepsilon$ final state. On-resonance a second channel becomes available from the $3d^8+3d^9\underline{L}$ ground state via the $2p^5 3d^9+2p^5 3d^{10}\underline{L}$ state in 2p XAS to the $3p^5 3d^8\varepsilon + 3p^5 3d^9\underline{L}\varepsilon$ final state. This resonance channel reaches exactly the same final states, which implies that both channels interfere. This resonance phenomenon is immediately clear if one plots the integrated 3p XPS intensity as a function of the excitation energy. This 3p-XPS detected 2p XAS spectrum shows a distortion of the normal 2p XAS spectral shape that best is known under the name Fano line shape.

Fig. 20 shows an example of such Fano behavior of resonant PES, as was reviewed in a recent paper by Martensson et al. [42]. The figure shows the 2p XAS spectrum of nickel metal, using the 2p3d3d resonant PES channel as detector. The $3d^7\varepsilon_A + 3d^8\underline{L}\varepsilon_A$ final state can be reached by the resonant channel and if only the resonant channel is available (and one would detect the complete decay spectrum) one would measure exactly the 2p XAS spectral shape. This experiment is an electron yield spectrum of 2p XAS. The $3d^7\varepsilon_A + 3d^8\underline{L}\varepsilon_A$ final state can however also be reached directly by photoemission. This direct channel is independent of the photon energy and by itself gives a constant background to the 2p XAS spectrum. However, we now have two channels that start from the same initial state and end at the same final states, implying interference effects. It can be shown that the consequence of such interference effect is the deformation of the 2pXAS spectral shape in a Fano-like fashion, as can be observed in Fig. 20. One can use such studies to study the amount of interference between various signals as a function of the decay energy and/or the angle [42].

Table 13
The configurations in resonant processes following, respectively, 2p XPS and a 2p XAS process

	Final state	Configurations	Spectroscopy
2p XPS	3d3d	$3d^6\varepsilon_A\varepsilon_P + 3d^7\underline{L}\varepsilon_A\varepsilon_P$	Normal XPS and Auger
	3p3d	$3p^5 3d^7\varepsilon_A\varepsilon_P + 3p^5 3d^8\underline{L}\varepsilon_A\varepsilon_P$	Possible to do APECS
$2p^5 3d^8\varepsilon_P + 2p^5 3d^9\underline{L}\varepsilon_P$	3p3p	$3p^4 3d^8\varepsilon_A\varepsilon_P + 3p^4 3d^9\underline{L}\varepsilon_A\varepsilon_P$	
	3s3d	$3s^1 3d^7\varepsilon_A\varepsilon_P + 3s^1 3d^8\underline{L}\varepsilon_A\varepsilon_P$	
	3s3p	$3s^1 3p^5 3d^8\varepsilon_A\varepsilon_P + 3s^1 3p^5 3d^9\underline{L}\varepsilon_A\varepsilon_P$	
	3s3s	$3s^0 3d^8\varepsilon_A\varepsilon_P + 3s^0 3d^9\underline{L}\varepsilon_A\varepsilon_P$	
2p XAS	3d3d	$3d^7\varepsilon_A + 3d^8\underline{L}\varepsilon_A$	Resonance with VB XPS
	3p3d	$3p^5 3d^8\varepsilon_A + 3p^5 3d^9\underline{L}\varepsilon_A$	Resonance with 3p XPS
$2p^5 3d^9 + 2p^5 3d^{10}\underline{L}$	3p3p	$3p^4 3d^9\varepsilon + 3p^4 3d^{10}\underline{L}\varepsilon_A$	3p3p RAES
	3s3d	$3s^1 3d^8\varepsilon + 3s^1 3d^9\underline{L}\varepsilon_A$	Resonance with 3s XPS
	3s3p	$3s^1 3p^5 3d^9\varepsilon_A + 3s^1 3p^5 3d^{10}\underline{L}\varepsilon_A$	3s3pRAES
	3s3s	$3s^0 3d^9\varepsilon_A + 3s^0 3d^{10}\underline{L}\varepsilon_A$	3s3sRAES

The second column gives the final state core holes.

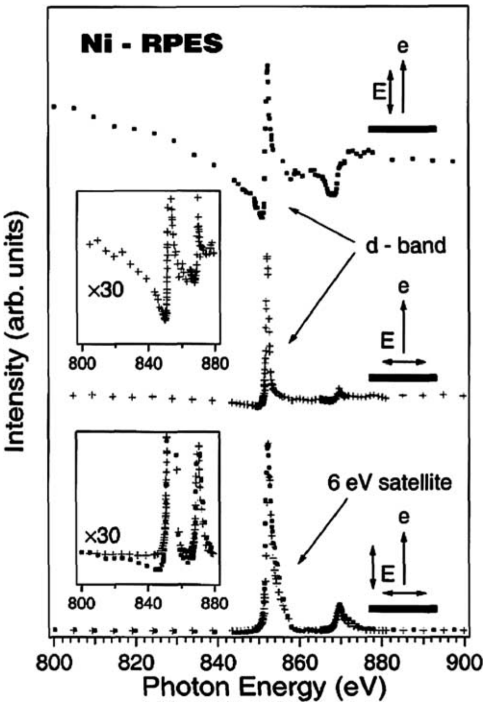

Fig. 20. Photoemission intensity of the valence band (top and middle curves) and the 6 eV satellite (bottom). The measurements have been made for two different directions of the *E*-vector of the incident radiation (reprinted with permission from [42], copyright 1999 Elsevier Science).

2.3.2. Resonant Auger

Apart from resonant photoemission one can also study the resonant Auger channels that cannot be reached directly from photoemission. These resonant Auger emission spectroscopy (RAES) lines can be used to combine the study of XAS and Auger spectra. This can be useful because XAS is sensitive to the symmetry, while Auger is more sensitive to the covalence. Fig. 21 shows the 3s3s, 3s3p and 3p3p RAES spectra of NiO measured at the peak maximum of the 2p XAS spectrum [41]. This study shows that when the excitation energy is below the L$_3$ resonance, one observes the 3p3p and 3s3p peaks at a constant binding energy, which is typical of resonant Auger. If the photon energy is increased further, the 3p3p and 3s3p lines transform into constant kinetic energy features, showing a normal Auger behavior. An interesting phenomenon is that on the high photon energy side of the 2p edge, the constant kinetic energy of the 3p3p and 3s3p peaks is systematically larger than the one observed for an excitation well above the edge. This is a direct consequence of the different final states that can be reached at resonance, as was indicated in Table 13, in particular the3d^{10} final states can be reached directly within a two-configuration description.

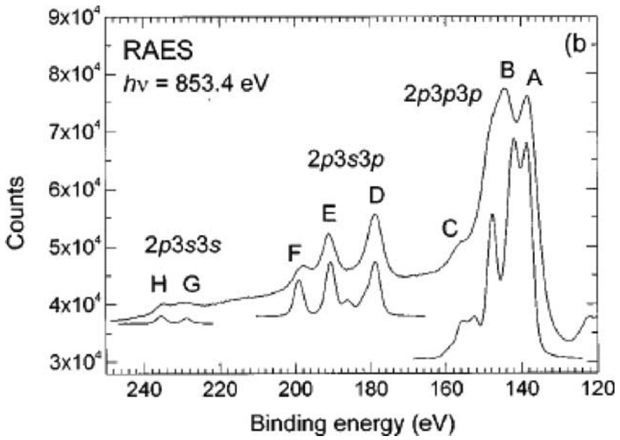

Fig. 21. The 2p3s3s, 2p3s3p and 2p3p3p RAES spectra of NiO (top) compared with a charge transfer multiplet calculation (bottom) as described in the text (reprinted with permission from [41], copyright 1999 American Physical Society).

It can be useful to study the whole interference effect in resonant photoemission and to map the complete two-dimensional energy space of photon energy in and electron energy out. This allows one, for example, to map the ratio of resonant versus normal Auger. Resonant Auger involves the excited electron in the Auger process, while normal Auger assumes a decoupling of the excitation and decay processes. A spectator channel assumes that the excited electron was decoupled from the core hole, and this process is strongly dependent on the hybridization of the atom that is excited with its neighbors. One can make use of this difference by studying the ratio of both processes under various conditions, for example, for adsorbates on metal surfaces. The resonant Auger channel is an atomic process involving local states. This implies that the resonant Auger is constant under various conditions. In contrasts the normal Auger channel is strongly affected by the hybridization and if one studies the ratio of both one finds a signal of the strength of hybridization of the atom with its environment. By using the decay time of the resonant channel, one can define a time scale for the delocalization of the excited electron and as such do ‘femtosecond spectroscopy’.

2.3.3. Auger photoemission coincidence spectroscopy

If one excites a system off-resonance one can still increase the amount of information beyond the normal XPS and Auger spectral shapes. The trick is to measure both spectra in coincidence. By doing so, one can study a single core excitation and decay process. Such Auger photoemission coincidence spectroscopy (APECS) experiments are difficult experimentally, but can in principal reveal additional information on the core hole process and on the electronic structure of the ground state. The description of APECS runs parallel with that of resonant photoemission and using Table 13, one can describe all transitions within the charge transfer multiplet model. A difference with resonant photoemission is that two electrons are excited, implying that different information is accessible. APECS experiments are not often performed and there are only a few published experiments on 3d-systems [43–46].

2.4. X-ray emission

X-ray emission is an old characterization technique. It traditionally made use of 1s2p X-ray emission and 1s3p X-ray emission channels, known as Kα and Kβ lines. One can divide the X-ray emission spectra into the hard X-ray spectra decaying to the 1s core hole and into soft X-ray spectra decaying into the 2p and other shallow core states. we will briefly mention a few aspects of such experiments.

2.4.1. 1s X-ray emission

Exciting a 1s core electron off-resonance creates a 1s core hole with a $1s^1 3d^8 \varepsilon + 1s^1 3d^9 L\varepsilon$ configuration. The1s2p X-ray emission replaces the 1s core hole with a 2p core hole, hence the final state can be written as $2p^5 3d^8 \varepsilon p + 2p^5 3d^9 L\varepsilon p$. This final state is equivalent to the final state in 2p XPS. In other words, one measures the same final states indirectly via 1s XPS followed by 1s2p XES. It should be noted that the spectral shapes of 1s2p XES is not the same as from 2p XPS because the transition matrices are different. In addition, the 1s core state could undergo 'relaxation' effects before the 2p to 1s decay occurs. Many details regarding such relaxation phenomena are still unknown.

Similar observations can be made for the 3p and valence states, as is indicated in Table 14. In this table CO stands for cross-over X-ray emission, i.e. the cross-over transition from a ligand 2s state to a metal 1s state, via the hybridization of the ligand 2s state with the metal 4p state. Bergmann et al. [47] have studied crossover transitions in detail. Valence band X-ray emission reaches the same final states as valence band photoemission, but again the matrix elements are different, and the dominating fluorescent decay channel is the valence band 4p to 1s decay. Because the 4p-charcater is strongly hybridized with the ligand valence states, one often apparently probes more the ligand states than the metal states.

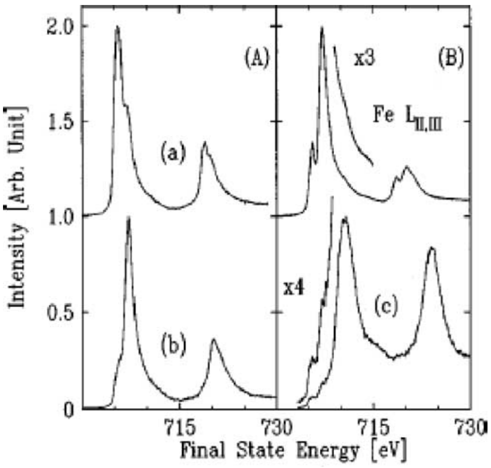

Fig. 22. Resonant XES spectra as a function of the energy difference of the incident and scattered photon energy (A). Together with the 2p XAS (B), the resonant XES spectra are given for three different excitation energies (a), (b) and (c) (reprinted with permission from [50], copyright 1998 American Physical Society).

Resonant excitations to the 1s XAS pre-edge modify the description of the X-ray emission channels considerable. The pre-edge peaks scan is dominated by the 1s to 3d quadrupole transitions [48]. This implies that the process is self-screened and the ordering of charge transfer states does not change. Performing 1s2p or 1s3p X-ray emission experiments at the pre-edge creates exactly the same final states as observed in a direct 2p, respectively, 3p XAS experiments. The transition matrix elements will be different, so the spectral shapes will look different. In fact, the spectral shapes will be different for each excitation energy. Fig. 22 shows the spectral shapes of Fe_2O_3, comparing the 1s2p pre-edge excited states (at two different energies in the pre-edge) compared with the direct 2p XAS spectrum. In general, it will be much easier to measure the 2p XAS spectrum, but the

Table 14
The configurations in resonant X-ray emission processes following, respectively, a 1s XPS, 1s XAS, a 2p XPS and a 2p XAS process

Intermediate state	Final state	Final state configurations	Related spectroscopy
1s XPS	2p	$2p^5 3d^8 \varepsilon p + 2p^5 3d^9 L\varepsilon p$	Kα (∼2p XPS)
$1s^1 3d^8 \varepsilon p + 1s^1 3d^9 L\varepsilon p$	3p	$3p^5 3d^8 \varepsilon p + 3p^5 3d^9 L\varepsilon p$	Kβ (∼3p XPS)
	CO	$L2s^1 3d^8 \varepsilon p + L2s^1 3d^9 L\varepsilon p$	Cross-over (via 4p)
	VB	$L2p^5 3d^8 \varepsilon p + L2p^5 3d^9 L\varepsilon p$	VB photoemission (via 4p)
1s $XAS_{\text{pre-edge}}$	2p	$2p^5 3d^9 + 2p^5 3d^{10} L$	Resonant Kα (∼2p XAS)
$1s^1 3d^9 + 1s^1 3d^{10} L$	3p	$3p^5 3d^9 + 3p^5 3d^{10} L$	Resonant Kβ (∼3p XAS)
	CO	$L2s^1 3d^9 + L2s^1 3d^{10} L$	Ligand 2s XAS cross-over
	VB	$L2p^5 3d^9 + L2p^5 3d^{10} L$	Ligand 2p VB XAS
2p XPS	3d	$3d^7 \varepsilon p + 3d^8 L\varepsilon_p$	VB photoemission
$2p^5 3d^9 L\varepsilon p$	3s	$3s^1 3d^8 \varepsilon p + 3s^1 3d^9 L\varepsilon p$	3s XPS
2p XAS	3d	$3d^8 + 3d^9 L$	Ground state + excitations
	3s	$3s^1 3d^9 + 3s^1 3d^{10} L$	3s XAS

The second column gives the final state core holes.

1s2p resonant XES spectrum allows the detection of the 2p XAS spectrum using only hard X-rays. This is important for in situ studies that are (with few exceptions) limited for soft X-rays. As was the case for resonant photoemission and APECS, also for resonant X-ray emission, it is possible to measure the complete two-dimensional spectral landscape of the combination of 1s excitation and 2p decay. This will be discussed in detail in the review by Glatzel and Bergmann elsewhere in this issue [49].

2.4.2. 2p X-ray emission

Experimentally, a soft X-ray emission experiment is quite different from hard X-ray emission experiment, in the first place due to the use of grating monochromators (for excitation and decay) compared to crystal monochromators. In addition, soft X-ray emission experiments are usually carried out in vacuum and they are usually measured with higher resolution, typically 0.3 eV for soft versus 1.0 eV for hard X-rays, though in principle hard X-ray experiments could be measured with a resolution of 0.3 eV.

Table 14 indicates that the valence band X-ray emission to the 2p core hole and performed at the 2p XAS edge, recreates the ground state plus low-energetic excitations. In other words, the 2p XAS followed by 2p3d XES amount to resonant elastic scattering. The fact that the ground state is regained with the creation and destruction of a core hole causes some special effects that can be used to gain new information. In particular, it was shown that low-lying magnetic excitations are visible in the 2p3d resonant XES spectrum.

Fig. 23 shows the resonant 2p3d XES spectra of NiO excited at five different energies as indicated on the right axis. Focusing on the total resonant XES signal, one observes at the excitation (just) below the edge the elastic excitation and the transition to the $^3T_2$ state, i.e. the first excited state in the 'Tanabe–Sugano diagram' of NiO. Note that this peak is the dominant transition in optical absorption spectroscopy. If one excites at 858 eV, i.e. at the shoulder in the NiO absorption spectrum, one observes a range of new peaks. The higher crystal field excitations gain intensity and two extra peaks are visible at, respectively, 0.25 and 1.25 eV. These extra peaks have a magnetic origin and they are due to spin-flip excitation of the Ni atom from $m_s = -1$ to $+1$. In these transitions one flips two spins, but this is possible due to the fact that the intermediate state has a core hole that has strongly coupled spin and orbital moments, i.e. a large spin–orbit coupling. This effectively allows these $\Delta m_s = 2$ spin-flip transitions to occur in resonant XES. The energy of this spin-flip transition is given by the energy it costs to flip a spin-state from antiferromagnetic to ferromagnetic, i.e. it is closely related to the superexchange energy in NiO [51]. If one excites at energies above the lowest 2p XAS excitations, one runs into the same situation as with resonant PES that there will be an addition of resonant and non-resonant XES spectra visible, potentially complicated with (incomplete) relaxation effects. Much is still unknown about the details of the processes taking place in the various systems, such as metals, adsorbates, single atoms, etc.

It is clear that if such 2p3d resonant XES experiments could be performed with the resolution as indicated in Fig. 23 (i.e. 0.2 eV overall), it would create a powerful new spectroscopic tool to study magnetic interactions in bulk magnetic oxides, magnetic nanoparticles and, for example, binuclear magnetic centers.

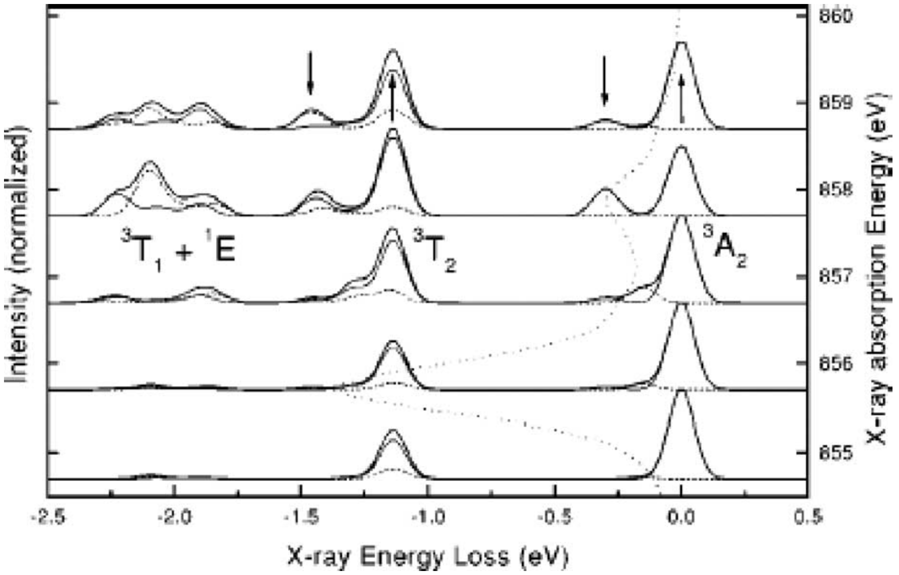

Fig. 23. Resonant 2p3d XES at the 2p edge of NiO. Indicated are F_{xx} scattering (thin solid), F_{zx} scattering (dashed), and the total scattering (thick solid). The X-ray-absorption spectrum is given with dots. The normalized resonant 2p3d XES spectra are given at the respective X-ray-absorption energies in steps of 1.0 eV as indicated on the right. The symmetries of the states are given at the middle spectrum (reprinted with permission from [51], copyright 1998 American Chemical Society).

In addition to the basic experiments described, a range of related experiments are possible. One can make use of the polarization of the X-rays, for example, with MCD experiments. Also one can detect the spin of the electrons in spin-polarized measurements. Another range of applications use the angular variations in the respective experiments. this includes polarization dependent XAS, including magnetic linear dichroism, polarization dependent resonant XES and angle-resolved photoemission. Experiments combining diffraction and absorption, for example, diffraction absorption fine structure (DAFS) or anomalous diffraction (MAD) must include multiplet effects if they play a role in the resonance used.

3. Examples for 3d coordination compounds

We end this review with a short overview of the various possibilities that are provided by the spectroscopic techniques discussed above, again with the focus on multiplet effects in the spectral shapes. We start with two examples that make use of the 1s XAS spectral shape, before turning to the soft X-ray 2p XAS spectra and the other spectroscopies.

3.1. The 1s XAS pre-edge shapes of coordination complexes

It was discussed above that the pre-edge region of the 1s XAS spectrum is dominated by the direct 1s to 3d quadrupole transitions. The pre-edge region of coordination compounds of iron has systematically been investigated by Westre et al. [48]. Analysis showed that the spectra should be interpreted in terms of multiplet theory, including the crystal field and the atomic interactions. That the pre-edge region in the case of Fe_2O_3 is almost completely of quadrupole nature can also be shown from 1s2p resonant X-ray emission experiments [50]. From the experiments, detailed information of iron in a range of complexes was obtained. This included the spin state, oxidation state, electronic structure parameters such as the crystal field splitting and hybridization effects, and indirectly also information on the geometry and for binuclear complexes also the bridging ligation.

It should be noted that there is no uniform understanding of the pre-edge spectral shapes. For example, detailed calculations on TiO_2 arrive at a slightly different model compared with the iron pre-edges discussed above. The pre-edge of TiO_2 has three pre-peaks that are caused by two effects: (1) the crystal field splitting between the T_{2g} and E_g orbitals and (2) the core hole effect on the quadrupole peaks shifting them by 2.5 eV with respect to the dipole peaks. The dipole peaks do not shift because they are related to 4p-character that overlaps with the 3d-bands of the neighbors. This assignment is confirmed by a number of detailed multiple scattering and band structure calculations [18,52]. Note that it is different from the usual assumption that the dipole and quadrupole peaks are positioned at the same energy.

3.2. The 1s XAS pre-edge intensity and energy of minerals

Waychunas did show for a series of minerals that a distortion of the octahedron will show up as an increased intensity of the pre-edge peak(s) [53]. They show a roughly linear relationship between the bond angle variance (a measure of the distortion) and the pre-edge intensity relative to the step. A detailed analysis of the pre-edge intensity and relative energy position was developed by Farges et al. [54]. From the analysis of a large number of titanium and iron compounds, the intensity and position of the pre-edge has been determined, where the center-of-gravity (f_1) is chosen for the determination of the position. Concerning the iron K edges, the f_1 energy position of Fe^{III} is 7113.5 eV both for tetrahedral and octahedral symmetry, while their relative intensities are, respectively, 0.35 for tetrahedral and 0.06 for octahedral symmetry. The main difference is the much larger dipole contribution to the tetrahedral site. A similar phenomenon can be observed for Fe^{II}, which leads to a tool to analyze both the valence and symmetry of iron sites from the pre-edge. This analysis technique has also been used for in situ studies of heterogeneous catalysts [55].

3.3. The 2p XAS and EELS of coordination compounds and proteins

The crystal field multiplet theory and later the charge transfer multiplet theory were developed originally for the 2p XAS spectra of transition metal oxides. The differences between the spectral shapes 2p XAS and 2p XPS have often been discussed [12,56]. In contrast to 2p XPS, the 2p XAS spectra are dominated by symmetry effects, while for monovalent and divalent oxides and halides covalence effects and the related charge transfer effects are much less important. These charge transfer multiplets effects effectively create only small satellites and compress the multiplet lines, in a manner equivalent to the nephelauxatic effects in UV-Vis spectroscopies.

The first systematic application of 2p XAS to coordination compounds was reported in 1991 by Cramer et al. [34]. They analyzed a range of manganese halides and manganese complexes. A systematic analysis revealed that it possible to readily determine the valence, spin-state and cubic crystal field strengths. It was shown that the final state crystal field splittings were reduced by 10% with respect to their optical analogs. This is due to the fact that the core hole potential is slightly larger than the 3d3d correlation energy U, i.e. the same effect that makes the charge transfer energy Δ slightly smaller in the final state. With the development of charge transfer multiplet theory, it became possible to analyze the 2p XAS spectra of trivalent and tetravalent oxides. At this moment 2p XAS has been developed into a standard characterization technique for new materials and nanoparticles, both at synchrotrons and with transition electron microscopes using EELS.

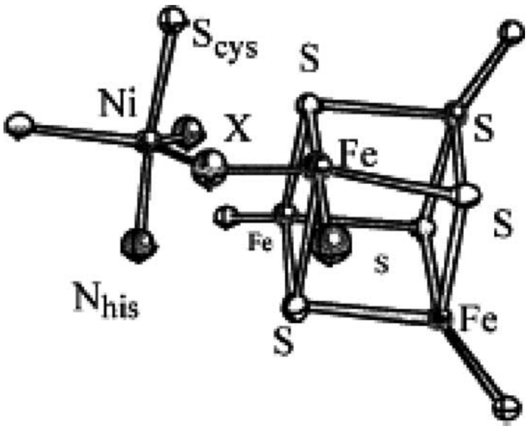

Fig. 24. Essential features of the Ni–X–Fe_4S_4 structures that have been proposed for CODH (reprinted with permission from [61], copyright 2000 American Chemical Society).

Hitchcock's group is well known for their core level EELS studies, in particular on organic molecules [57]. We would like to mention their study on iron-carbonyl and iron–ferrocene complexes in the early nineties [58,59]. At that time the multiplet model was just being developed and charge transfer not yet included. In addition, multiplet theory (in its simplest form) is best suited to describe oxides and halides. In particular the ferrocene have little resemblance to the ligand field multiplet spectra, as they would need a much better description of the covalence effects and of π-(back)bonding. These effects are not yet included into the multiplet model, though some progress is being made as will be discussed below.

The group of Cramer applied 2p XAS including its MCD effect to metallo-enzymes and related model compounds [60–63]. The MCD experiments are discussed in the review of Cramer, elsewhere in this issue. As an example, the 2p XAS spectra of Carbon monoxide dehydrogenase from *Clostridium thermoaceticum* (Ct, CODH) and *Rhodospirillum rubrum* (Rr, CODH) will be discussed [61] (Fig. 24).

The electronic structure of the nickel site in this enzyme is studied in comparison with a large number of model compounds. The 2p XAS spectra of the model compounds are analyzed taking two parameters as measure (1) the center-of-gravity of the L_3 edge and (2) the branching ratio. The branching ratio is defined as the integrated intensity of the L_3 edge divided by the integrated intensity of the whole 2p XAS spectrum, i.e. the L_3 and L_2 edge added. The value of the branching ratio without multiplets is 2/3, given by the degeneracy of the L_3 and L_2 edges. Because the multiplet effects are of the same order of magnitude as the 2p spin–orbit coupling the branching ratios are modified by multiplet effects, and the details of the effect are strongly influenced by the spin state of the metal. This makes the branching ratio to a tool to determine the spin state of transition metals, as can be seen from Fig. 25.

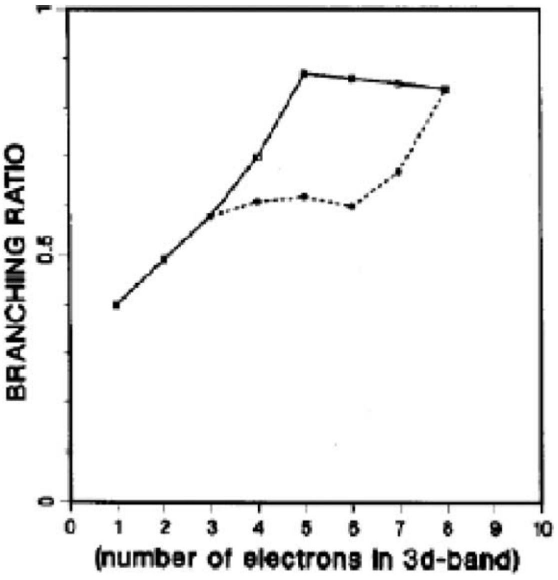

Fig. 25. The branching ratio of transition metal ions (given by their formal number of 3d-electrons) as predicted from crystal field multiplet theory. High-spin states are given by the solid line; low-spin is given by the dashed line. This picture will be modified by lower symmetries and charge transfer (reprinted with permission from [12], copyright 1994 Elsevier Science).

From Fig. 25, it can be observed that the early transition metal ions have branching ratios that are strongly deviating from 2/3 and that low-spin compounds have relatively large L_2 edges. MnO and other $3d^5$ compounds have the highest branching ratio of approximately 0.85.

Fig. 26 shows the analysis of the nickel model compounds for their energy position and branching ratio. It can be seen that the various valences and spin-states can be dis-

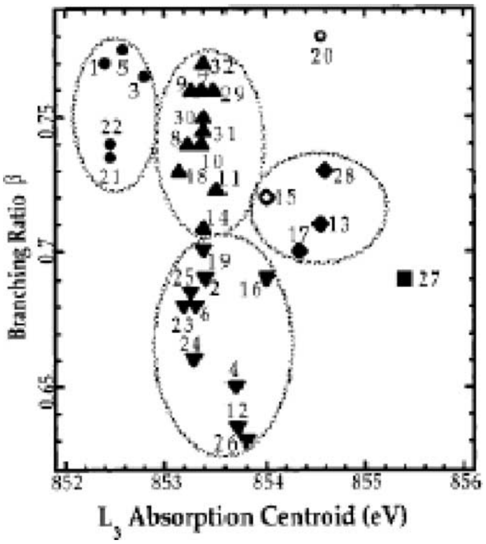

Fig. 26. Two-dimensional correlation of branching ratio vs. L_3 centroid position for a set of Ni model compounds with different oxidation state and spin states. Key: Ni^{I} filled circles; low-spin Ni^{II} inverted triangles; high-spin Ni^{II} upright triangles; low-spin Ni^{III} black diamonds; high-spin Ni^{III} open circle; Ni^{IV} square. Ellipses are drawn only to guide the eye (reprinted with permission from [61], copyright 2000 American Chemical Society).

tinguished by the energy position and branching ratio analysis. In addition, it is clear that there is a significant variation within each group. These variations are due to differences in the local symmetry and covalence. The 2p XAS spectra of CODH indicate that most of the Ni in as-isolated Ct-CODH is low-spin Ni^{II}. Upon CO treatment, a fraction of the nickel is converted either to high-spin Ni^{II} and/or to Ni^{I}. Ni in dithionite-reduced Rr-CODH also exhibits a clear low spin Ni^{II} component, again mixed with either high-spin Ni^{II} or Ni^{I}. The spectrum of Rr-CODH shifts to higher energy upon oxidation, suggesting either that most of the high-spin Ni^{II} is converted to low-spin Ni^{II} and/or that some Ni is oxidized between these two forms.

A number of 2p XAS studies on coordination compounds, including nickel dithiocarbamate complexes, vanadium with oxyoxime ligands and iron with bidentate *N*-donor ligands have been performed by the groups of Garner and co-workers [64–66]. An interesting study is on nickel dithiocarbamate and xanthate complexes, where it is shown that the 2p XAS experiments induce photoreduction of such nickel complexes, for example, modifying $[Ni^{IV}(S_2CNEt_2)_3][BF_4]$ into a Ni^{II} square-planar species. Similar phenomena were often observed for many X-ray sensitive compounds that have been measured at the most intense X-ray sources, with the implication that the measurements always have to be checked for sample damage. Because this is an important issue, some of the results on the nickel dithiocarbamate complexes will be discussed.

Fig. 27 shows the gradual change from an octahedral Ni^{IV} center to a square planar Ni^{II} center under irradiation, where the final spectrum was reached after 3 h. Similar effects were found on a range of samples and it was found that the decay rate is dependent on photon flux, photon energy and ligand set, but is independent of temperature [66]. In case of metallo-enzymes, it is well known that they are unstable and for those systems measurements at low temperature (4 K) also seemed to be better concerning radiation damage compared with, for example, 77 K. In Fig. 26, the changes were gradual and slow. It can be expected that more sensitive systems will even decay within seconds, which implies that even the first spectrum is already taken on a modified sample. In case one expects radiation effects, one should do its best to take a first spectrum in a short time, ideally in a matter of seconds, thereby strongly limiting the possibility that one measures a spectrum of an already damaged sample.

Arrio and co-workers have analyzed a number of metal complexes in detail, using the charge transfer multiplet model [67–70]. An important addition to the multiplet model was the treatment of π-(back)bonding, i.e. metal to ligand charge transfer (MLCT). The charge transfer multiplet model had been developed with respect to solid state transition metal oxides that are dominated by σ-bonding and by ligand to metal charge transfer (LMCT), i.e. the addition of $3d^9L$ configurations to a $3d^8$ ground state (for Ni^{II} systems). Arrio and co-workers studied molecular-based magnets $Cs[Ni^{II}Cr^{III}(CN)_6]–2H_2O$, $Co^{II}3[Cr^{III}(CN)_6]_2–12H_2O$, $Fe^{II}3[Cr^{III}(CN)_6]_2–18H_2O$, and $Cs[Mn^{II}Cr^{III}(CN)_6]–2H_2O$. These systems are cubic with the CN groups bridging two transition metal sites. The carbon is bonded to the Cr^{III} and the nitrogen to the divalent Ni, Co, Fe and Mn sites. The divalent octahedral nitrogen bonded sites are all high-spin and the 2p XAS spectra of these sites can all be simulated nicely with the charge transfer multiplet model using LMCT, for example, the Ni^{II} site has a ground state of 90% $3d^8$ and 10% $3d^9L$ character. In contrast, the Cr^{III} sites could not be described

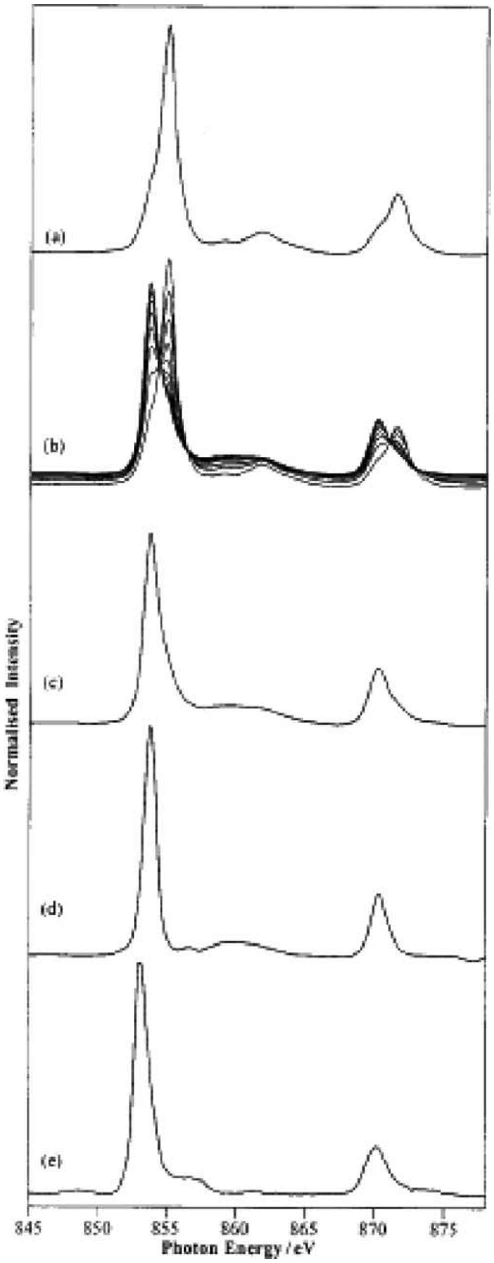

Fig. 27. Ni L-edge spectra of (a) $[Ni^{IV}(S_2CNEt_2)_3][BF_4]$ initial spectrum; (b) $[Ni^{IV}(S\ CNEt_2)_3][BF_4]$ successive spectra; (c) $[Ni^{IV}(S_2CNEt_2)_3][BF_4]$ final spectrum; (d) $[Ni^{II}(S_2CNEt_2)_2]$; and (e) $[PPh_4][Ni^{II}(SCOEt)_3]$ (reprinted with permission from [66], copyright 1998 Royal Society of Chemistry).

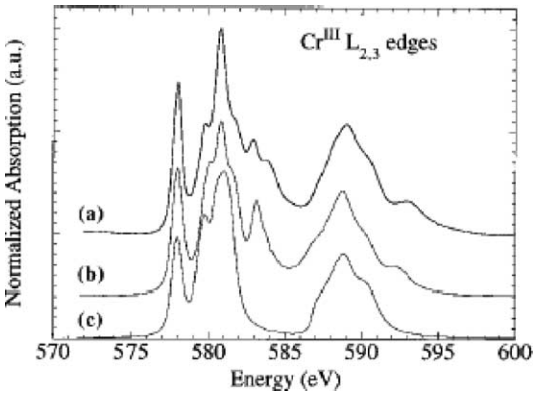

Fig. 28. (a) Experimental Cr^{III} 2p XAS spectrum. (b) Theoretical Cr^{III} 2p XAS spectrum calculated with the $3d^3 + 3d^2L$ interaction configuration. (c) Theoretical Cr^{III} 2p XAS spectrum calculated with 10Dq) 3.5 eV and the Slater integrals reduced to 50% and no configuration interaction (reprinted with permission from [67], copyright 1996 American Chemical Society).

adequately with MLCT and the calculations using $3d^3$ with $3d^4\underline{L}$ character all failed to describe the 2p XAS spectrum. The problem is that, besides LMCT, there is also MLCT. In principle, one should include both effects in the calculations, but to limit the calculation, it was decided to include the LMCT by reducing the Slater integrals and to include the $3d^2L$ configuration describing MLCT, explicitly.

Fig. 28 shows that this model gave a good description of the spectral shape of the Cr^{III} sites. In particular the structure at 583 eV is shown to originate from the MLCT to the cyanide. This phenomenon is generally confirmed for π-(back)bonding systems.

A beautiful example of the application of the charge transfer multiplet model are the 2p XAS and MCD measurements and simulations of two paramagnetic high-spin molecules $Cr\{(CN)Ni(tetren)\}_6](ClO_4)_9$ and $[Cr\{(CN)Mn(TrispicMeen)\}_6]–(ClO_4)_9$, 3THF (Fig. 29). The 2p XAS and X-MCD spectra were calculated in the charge transfer multiplet model. The Mn^{II} sites were again found to be weakly covalent with some LMCT, while the Cr^{III} sites again are affected by MLCT and the $3d^3 + 3d^2L$ calculation yields a good description of the spectrum. In particular the X-MCD spectral shape is near perfectly reproduced, indicating that the two-state model is adequate to describe the present system. Comparing the sign of the X-MCD with the calculations, one finds that the Mn^{II} sites are antiferromagnetically coupled to the Cr^{III} sites.

An often studied system is $[Fe^{II}(phen)_2(NCS)_2]$ (phen = 1,10-phenanthroline), which is well known for its spin-flip behavior under external conditions. The octahedral Fe^{II} sites change their spin, for example, as a function of temperature, from high-spin S = 2 to low-spin S = 0, i.e. two electrons flip their spin states. This system was often studied with X-ray spectroscopic techniques. Briois et al. used 1s XAS and 2p XAS. Ligand field multiplet analysis of the 2p XAS spectral shapes found large changes in the crystal field value that is reduced from 2.5 eV for low-spin to 0.5 eV for high-spin [68]. Collison and co-workers studied the same system and performed soft X-ray induced spin transitions by trapping the excited spin state. They performed a detailed study of the 2p XAS spectra as a function of temperature and X-ray excitation energies, thereby creating second high-spin state different from the original [66]. Recently, Vanko has studied the same system using 1s2p and 1s3p resonant XES [71].

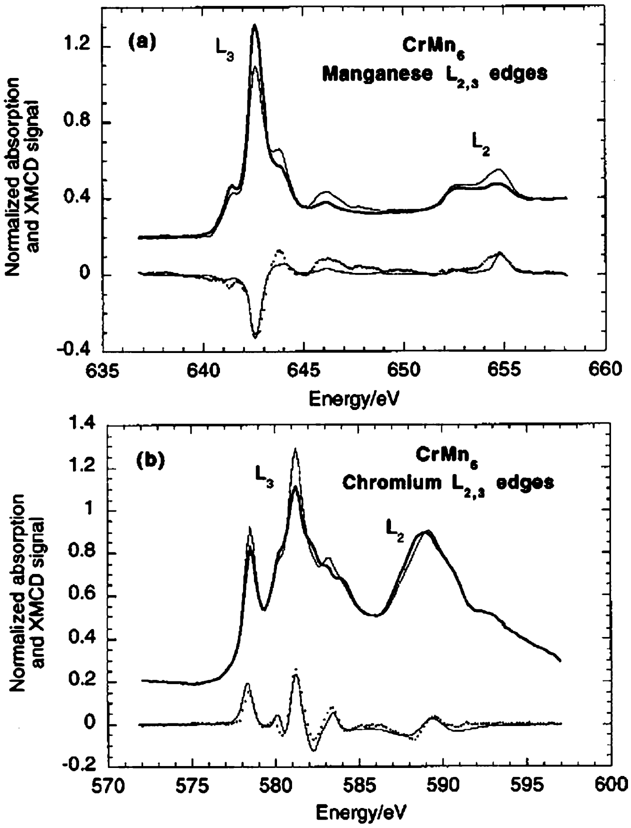

Fig. 29. (a) Experimental Mn 2p XAS spectrum of $[Cr\{(CN)Mn(TrispicMeen)\}_6](ClO_4)_9$,3THF, paralel (thick line) and anti-parallel (thin line) (top). Experimental (dots) and theoretical (line) X-MCD signal normalized to 100% circular polarized light (bottom). (b) The Cr 2pXAS and X-MCD spectra (reprinted with permission from [69], copyright 1999 American Chemical Society).

3.4. The differential orbital covalence derived from 2p XAS

The charge transfer multiplet analysis of 2p XAS and other spectroscopies gives good simulations on the spectral shape, but on the other hand, it makes a direct understanding of the spectral shape difficult. Fig. 11 showed that it can be useful to turn off the multiplet effects once a good simulation was obtained. By turning off the multiplet effects one obtains the one-electron analog of the 2p XAS spectrum. Wasinger et al. have followed a similar approach recently [72]. They extended the charge transfer multiplet theory, to derive the differential orbital covalence (DOC) directly from the 2p XAS spectral shape analysis (Fig. 30).

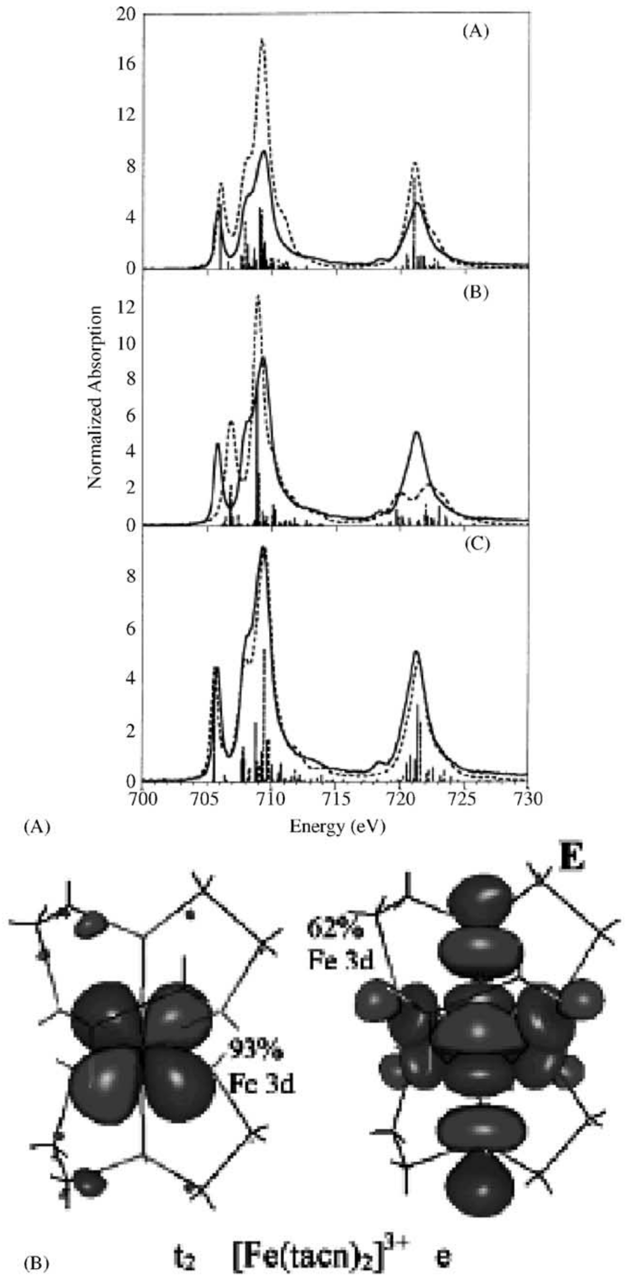

Fig. 30. Left (from top to bottom): ligand field multiplet (A); isotropic covalence charge transfer multiplet (B); and DOC charge transfer multiplet (C) simulations of Fe(tacn)$_2{}^{3+}$. Right: the single particle analysis obtained by removing the 2p3d multiplet effects and all 3d3d correlation effects from the $3d^5 + 3d^6\underline{L}$ ground state. The Contour plots of the antibonding metal t_{2g} (left) and e_g (right) orbitals have been calculated with DFT (reprinted with permission from [72], copyright 2003 American Chemical Society).

Fig. 30 shows the 2p XAS spectral shape of the low-spin ferric complex Fe(tacn)$_2{}^{3+}$. The top spectrum is simulated with a pure $3d^5$ ground state, with 10Dq = 2.50 eV and a Slater integral reduction of 65%, in agreement with optical data. The energy splittings are found to be in reasonable agreement between the multiplet simulation and the data. However, the simulation significantly overestimates the intensity of all of the L_3 and L_2 pre-edge features. The mismatch in simulated intensity to the data indicates the inadequacy of the ligand field multiplet method to model the ground state wave function of [Fe(tacn)$_2$]$^{3+}$. As discussed above, the inclusion of charge-transfer adds a $3d^6\underline{L}$ configuration to the $3d^5$ ground state. The charge transfer multiplet model as introduced in Section 1.5 for NiO assumed a constant ratio between the t_{2g} and e_g orbitals of 1–2, mimicking the octahedral surroundings of Ni in NiO. In Fig. 26 the charge transfer effect is introduced in two steps, first the same mixing is used for t_{2g} and e_g orbitals (middle spectrum), and then the independent mixings for the t_{2g} and e_g orbitals are optimized to mimic best the experiment. This yield a mixing of 0.4 for the e_g electrons and of 0.9 for the t_{2g} electrons. These numbers translate to a DOC of 99% for the t_{2g} electrons and of 63% for the e_g electrons, in close agreement with DFT calculations. The DOC numbers are calculated from the $3d^5$+$3d^6\underline{L}$ ground state, using the charge transfer parameters as determined from the simulation, and calculating the corresponding ground state wave function by turning the 3d3d correlations and 3d spin–orbit coupling to zero [72].

3.5. The 2p XPS spectrum of Cu(acac)$_2$

Multiplet analysis of XPS spectra of coordination compounds is not often performed. Still, 2p XPS, for example, in combination with 2p XAS, could provide very useful information on the chemical bonding. A beautiful extension of charge transfer multiplet theory was presented by Okada et al. in their analysis of the 2p XPS spectrum of Cu(acac)$_2$ [73] (Fig. 31). The spectrum of this Cu^{II} compound has three peaks, which is not expected for a $3d^9$ compound, because the ground state is expected to consist of $3d^9$ and $3d^{10}\underline{L}$ configurations only, leaving for the final state only two charge transfer states $2p^5 3d^9$ and $2p^5 3d^{10}\underline{L}$. The $2p^5 3d^{10}\underline{L}$ state is a single peak and the $2p^5 3d^9$ state gives some multiplet splitting but this is of the order of a approximately 2 eV, while the experimental spectrum has two satellites split by about 6 eV.

The solution to this problem came with the realization that the oxygen 2p valence band energy positions of the $2p_x$ versus the $2p_y$ states are shifted by about 5 eV. This implies that the $3d^9$ ground state mixes with two distinct $3d^{10}\underline{L}$ states. Within the charge transfer multiplet model this implies the usage of two different Δ's. The energy scheme reveals that one of these $3d^{10}\underline{L}$ state forms the main contribution to the leading peak, while the other one forms a satellite, while the second satellite relates mostly to the$3d^9$ final state. This models is able to explain the observed spectral shape exactly.

3.6. Valence, site, spin and symmetry selective XAS

We would like to give one example of the use of multiplet theory in X-ray emission. The example makes use of the

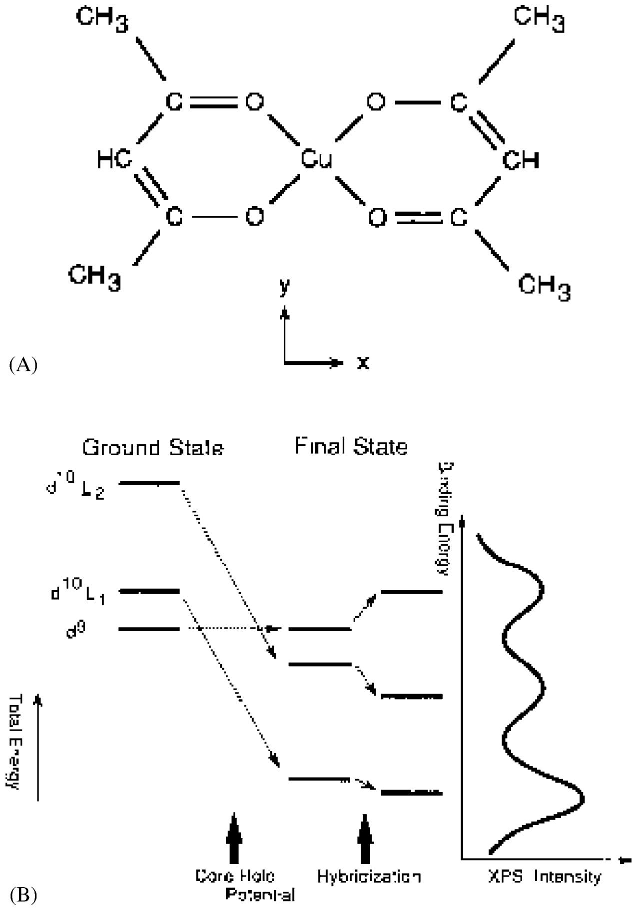

Fig. 31. The structure of Cu(acac)$_2$ (left). The mixing of the 3d^9 configuration with the two 3d^{10}L configuration in the initial and final state (right) (reprinted with permission from [73], copyright 1993 American Physical Society).

multiplet effects the final state of an 1s3p XES experiment. By making use of these multiplet splittings, it is possible to distinguish different valences in the emission spectrum. Using a high-resolution detector, this allows to measure independently the spectra of two different valences in a mixed valence compound (Fig. 32).

Valence selective X-ray absorption was applied to $Fe_4[Fe(CN)_6]_3 \cdot xH_2O$ ($x = 14$–16), i.e. Prussian Blue (PB) [74]. Fig. 32 shows that the 1s3p XES spectra of Fe_2O_3 and $K_4Fe(CN)_6$, respectively, high-spin Fe^{III} and low-spin Fe^{II} compound, are shifted in energy with respect to each other. It is noted that the center of gravity of the Fe^{III} and Fe^{II} 1s3p XES spectra are NOT shifted with respect to each other, because one measures a transition from one core state (1s) to another core state (3p), and the respective energy differences between these ore state are equal independent of the situation around the valence states. The fact that still a shift is observed in the experiment is due to multiplet effects, i.e. the exchange interaction between the 3p final state and the 3d-states is very large and creates the satellites at 7040 eV, split by about 20 eV from the main peak. The peak splitting and the amount of intensity shifted to this satellite is strongly dependent on the valence and spin-state. This difference implies that the main peak will also have to shift to keep the center of gravity fixed. It is this multiplet-induced shift that makes the1s3p XES spectra suitable for valence selective XAS studies. Note that the1s2p XES is less suitable because the 2p3d exchange splitting is much smaller and one expects much smaller shifts in the peak maxima of a 1s2p spectrum. The 1s XANES and EXAFS were measured at various energy positions and using a numerical method, the individual site EXAFS spectra were extracted from the experimental data [80]. The pre-edge and XANES regions are affected by more complex resonance effects that are discussed in the review by Glatzel and Bergmann elsewhere in this issue [49].

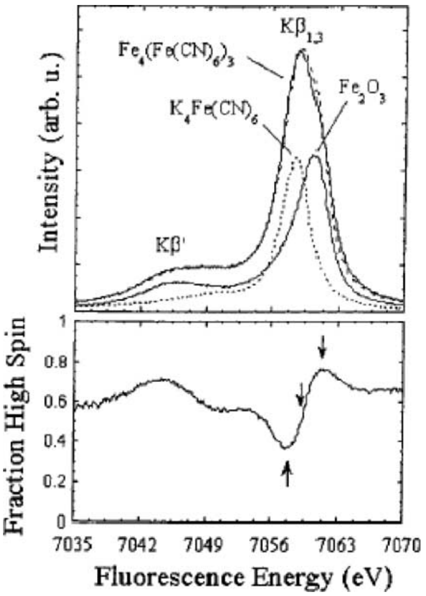

Fig. 32. Top: lower curves: K, spectra of Fe_2O_3 (solid line) and $K_4Fe(CN)_6$ (dotted line). Upper curves: $Fe_4[Fe(CN)_6]_3$ spectrum (solid line) vs. normalized sum of Fe_2O_3 and $K_4Fe(CN)_6$ spectra (dashed line). Lower panel: fraction of signal arising from high-spin Fe^{III} component in the PB spectrum vs. fluorescence energy, using Fe_2O_3 and $K_4Fe(CN)_6$ as models. The arrows indicate the fluorescence energies where site-selective absorption spectra were taken (reprinted with permission from [74], copyright 2000 American Chemical Society).

Instead of using chemical shifts due to valence differences of two states, one can make use any variable that caused a different decay spectrum, either via electrons, i.e. Auger or via photons, i.e. XES. In principle, an enormous range of possibilities can be used, including the use of secondary or cascade decay products, for example, X-ray excited optical luminescence (XEOL)signals, etc. Each signal will have its own characteristic with respect to probing depth, detection area, etc. for example, 1s2p XES will be a local probe, whereas optical signals (XEOL) will emit from a large (*r*) area around the absorbing atom, etc.

A beautiful example, using soft X-ray emission is the detection of the independent 1s XAS spectra of N_2 molecule adsorbed on a nickel surface. By detecting specific decay channels of the nitrogen bonded to the surface one can measure the 1s XAS spectrum of only this atom [42]. Another selectivity can be obtained towards the spin of the absorbing atom. A spin-up core hole will interact differently than a spin-down core hole with the valence spins, and it is relatively easy to show that the 1s2p and 1s3p XES signals have a completely different spectral shape for spin-up and spin-down. These processes are local and as such one is measuring local spin states, i.e. for an antiferromagnet and a paramagnet one will measure also a spin-selective signal [75–78].

4. Outlook

In this review I have given an overview of the use of multiplet effects in X-ray spectroscopy, with an emphasis on X-ray absorption experiments of coordination compounds. It can be expected that this field will further develop in the years to come. In particular multiplet theory is still in its infancy with regard to the complete description of the chemical bonding in coordination complexes and aspects such as π-bonding and back bonding should be better described. This also implies a more general description of the ground state of the systems and ideally a unified description of 2p X-ray absorption and its dichroism, in combination with experiments such as EPR and optical dichroism.

On the experimental side a range of new experimental techniques is being developed, in particular with respect to measurements under extreme conditions and under working conditions of, for example, catalysts and electrochemical cells. A beautiful new experiment is the photo-excited picosecond X-ray absorption experiment [79] that will be applied to transitions metal edges.

References

[1] J.J. Rehr, R.C. Albers, Rev. Modern Phys. 72 (2000) 621.
[2] J.J. Rehr, A.L. Ankudinov, J. Synchrotron Radiat. 8 (2001) 61.
[3] M. Taillefumier, D. Cabaret, A.M. Flank, F. Mauri, Phys. Rev. B (2002) 66, art. no. 195107.
[4] F.M.F. Degroot, Physica B 209 (1995) 15.
[5] Z. Hu, H. Von Lips, M.S. Golden, J. Fink, G. Kaindl, F.M.F. Degroot, S. Ebbinghaus, A. Reller, Phys. Rev. B 61 (2000) 5262.
[6] M. Finazzi, N.B. Brookes, F.M.F. Degroot, Phys. Rev. B 54 (1999) 9933.
[7] P.H. Butler, Point Group Symmetry Applications: Methods and Tables, Plenum Press, New York, 1981.
[8] M. Weissbluth, Atoms and Molecules, Plenum Press, New York, 1978.
[9] Z. Hu, G. Kaindl, S.A. Warda, D. Reinen, F.M.F. Degroot, B.G. Muller, Chem. Phys. 232 (1998) 63.
[10] Z. Hu, C. Mazumdar, G. Kaindl, F.M.F. Degroot, S.A. Warda, D. Reinen, Chem. Phys. Lett. 297 (1998) 321.
[11] S. Sugano, Y. Tanabe, H. Kamimura, Multiplets of Transition Metal Ions, Academic Press, New York, 1970.
[12] F.M.F. Degroot, J. Electron Spectrosc. Relat. Phenomena 67 (1994) 529.
[13] F.M.F. Degroot, J.C. Fuggle, B.T. Thole, G.A. Sawatzky, Phys. Rev. B 42 (1990) 5459.
[14] F.M.F. Degroot, J.C. Fuggle, B.T. Thole, G.A. Sawatzky, Phys. Rev. B 41 (1990) 928.
[15] F.M.F. de Groot, Ph.D. thesis, 1991.
[16] K. Okada, A. Kotani, J. Phys. Soc. Jpn. 61 (1992) 449.
[17] K. Okada, A. Kotani, J. Phys. Soc. Jpn. 61 (1992) 4619.
[18] T. Uozumi, K. Okada, A. Kotani, J. Phys. Soc. Jpn. 62 (1993) 2595.
[19] F.M.F. Degroot, M.O. Figueiredo, M.J. Basto, M. Abbate, H. Petersen, J.C. Fuggle, Phys. Chem. Minerals 19 (1992) 140.
[20] M.O. Figueiredo, A.C. Dos Santos, M.F. Melo, F.M.F. de Groot, M. Abbate, Adv. Sci. Technol. 3B (1995) 733.
[21] F.J. Himpsel, U.O. Karlsson, A.B. Mclean, L.J. Terminello, F.M.F. Degroot, M. Abbate, J.C. Fuggle, J.A. Yarmoff, B.T. Thole, G.A. Sawatzky, Phys. Rev. B 43 (1991) 6899.
[22] J. Hasselstrom, A. Fohlisch, R. Denecke, A. Nilsson, F.M.F. Degroot, Phys. Rev. B 62 (2000) 11192.
[23] T. Jo, A. Kotani, J. Phys. Soc. Jpn. 57 (1988) 2288.
[24] O. Gunnarsson, K. Schönhammer, Phys. Rev. B 28 (1983) 4315.
[25] A. Fujimori, F. Minami, Phys. Rev. B 30 (1984) 957.
[26] G.A. Sawatzky, J.W. Allen, Phys. Rev. Lett. 53 (1984) 2339.
[27] G van der Laan, J. Zaanen, G.A. Sawatzky, R. Karnatak, J.M. Esteva, Phys. Rev. B 33 (1986) 4253.
[28] J. Zaanen, G.A. Sawatzky, J.W. Allen, Phys. Rev. B 55 (1985) 418.
[29] K. Okada, A. Kotani, Physica B 237 (1997) 383.
[30] M.A. Vanveenendaal, G.A. Sawatzky, Phys. Rev. Lett. 70 (1993) 2459.
[31] F. Jollet, V. Ortiz, J.P. Crocombette, J. Electron Spectrosc. Relat. Phenomena 86 (1997) 83.
[32] R.H. Potze, G.A. Sawatzky, M. Abbate, Phys. Rev. B 51 (1995) 11501.
[33] K. Okada, A. Kotani, J. Phys. Soc. Jpn. 66 (1997) 341.
[34] S.P. Cramer, F.M.F. Degroot, Y. Ma, C.T. Chen, F. Sette, C.A. Kipke, D.M. Eichhorn, M.K. Chan, W.H. Armstrong, E. Libby, G. Christou, S. Brooker, V. Mckee, O.C. Mullins, J.C. Fuggle, J. Am. Chem. Soc. 113 (1991) 7937.
[35] S.M. Butorin, J. Electron Spectrosc. Relat. Phenomena 110 (2000) 213.
[36] P. Mahadevan, D.D. Sarma, Phys. Rev. B 61 (2000) 7402.
[37] C. De Nadai, A. Demourgues, J. Grannec, F.M.F. de Groot, Phys. Rev. B 63 (2001) xxx.
[38] K. Okada, A. Kotani, B.T. Thole, J. Electron Spectrosc. Relat. Phenomena 58 (1992) 325.
[39] M. Finazzi, N.B. Brookes, F.M.F. De Groot, Phys. Rev. B 59 (1999) 9933.
[40] K. Okada, A. Kotani, H. Ogasawara, Y. Seino, B.T. Thole, Phys. Rev. B: Condensed Matter 47 (1993) 6203.
[41] K. Okada, A. Kotani, V. Kinsinger, R. Zimmermann, S. Hufner, J. Phys. Soc. Jpn. 63 (1994) 2410.
[42] N. Martensson, O. Karis, A. Nilsson, J. Electron Spectrosc. Relat. Phenomena 100 (1999) 379.
[43] S.M. Thurgate, J. Electron Spectrosc. Relat. Phenomena 81 (1996) 1.
[44] S.M. Thurgate, J. Electron Spectrosc. Relat. Phenomena 100 (1999) 161.
[45] R.A. Bartynski, E. Jensen, S.L. Hulbert, C.C. Kao, Prog. Surf. Sci. 53 (1996) 155.
[46] M.T. Butterfield, R.A. Bartynski, S.L. Hulbert, Phys. Rev. B (2002) 66, art. no. 115115.
[47] U. Bergmann, J. Bendix, P. Glatzel, H.B. Gray, S.P. Cramer, J. Chem. Phys. 116 (2002) 2011.
[48] T.E. Westre, P. Kennepohl, J.G. Dewitt, B. Hedman, K.O. Hodgson, E.I. Solomon, J. Am. Chem. Soc. 119 (1997) 6297.
[49] P. Glatzel, U. Bergmann, CCR, 2004, this issue.
[50] W.A. Caliebe, C.C. Kao, J.B. Hastings, M. Taguchi, T. Uozumi, F.M.F. Degroot, Phys. Rev. B 58 (1998) 13452.
[51] F.M.F. Degroot, P. Kuiper, G.A. Sawatzky, Phys. Rev. B 57 (1998) 14584.

[52] D. Cabaret, Y. Joly, H. Renevier, C.R. Natoli, J. Synchrotron Radiat. 6 (1999) 258.
[53] G.A. Waychunas, Am. Mineral. (1987) 7289.
[54] F. Farges, G.E. Brown, J.J. Rehr, Phys. Rev. B: Condensed Matter 56 (1997) 1809.
[55] W.M. Heijboer, A.A. Battiston, A. Knop-Gericke, M. Hävecker, R. Mayer, H. Bluhm, R. Schlögl, B.M. Weckhuysen, D.C. Koningsberger, F.M.F. de Groot, J. Phys. Chem. B 107 (2003) 13069.
[56] G. Vanderlaan, J. Zaanen, G.A. Sawatzky, R. Karantak, J.M. Esteva, Phys. Rev. B 33 (1986) 4253.
[57] A.P. Hitchcock, M.J. Mcglinchey, A.L. Johnson, W.K. Walter, M.P. Jigato, D.A. King, D. Norman, E. Ruhl, C. Heinzel, H. Baumgartel, J. Chem. Soc., Faraday Trans. 89 (1993) 3331.
[58] A.P. Hitchcock, A.T. Wen, E. Ruhl, Chem. Phys. 147 (1990) 51.
[59] A.T. Wen, E. Ruhl, A.P. Hitchcock, Organometallics 11 (1992) 2559.
[60] S.P. Cramer, C.Y. Ralston, H.X. Wang, C. Bryant, J. Electron Spectrosc. Relat. Phenomena 86 (1997) 175.
[61] C.Y. Ralston, H.X. Wang, S.W. Ragsdale, M. Kumar, N.J. Spangler, P.W. Ludden, W. Gu, R.M. Jones, D.S. Patil, S.P. Cramer, J. Am. Chem. Soc. 122 (2000) 10553.
[62] H.X. Wang, D.S. Patil, W.W. Gu, L. Jacquamet, S. Friedrich, T. Funk, S.P. Cramer, J. Electron Spectrosc. Relat. Phenomena 114 (2001) 855.
[63] H.X. Wang, C.Y. Ralston, D.S. Patil, R.M. Jones, W. Gu, M. Verhagen, M. Adams, P. Ge, C. Riordan, C.A. Marganian, P. Mascharak, J. Kovacs, C.G. Miller, T.J. Collins, S. Brooker, P.D. Croucher, K. Wang, E.I. Stiefel, S.P. Cramer, J. Am. Chem. Soc. 122 (2000) 10544.
[64] D. Collison, C.D. Garner, J. Grigg, C.M. Mcgrath, J.F.W. Mosselmans, E. Pidcock, M.D. Roper, J.M.W. Seddon, E. Sinn, P.A. Tasker, G. Thornton, J.F. Walsh, N.A. Young, J. Chem. Soc., Dalton Trans. (1998) 2199.
[65] D. Collison, C.D. Garner, C.M. Mcgrath, J.F.W. Mosselmans, E. Pidcock, M.D. Roper, B.G. Searle, J.M.W. Seddon, E. Sinn, N.A. Young, J. Chem. Soc., Dalton Trans. (1998) 4179.
[66] D. Collison, C.D. Garner, C.M. Mcgrath, J.F.W. Mosselmans, M.D. Roper, J.M.W. Seddon, E. Sinn, N.A. Young, J. Chem. Soc., Dalton Trans. (1997) 4371.
[67] M.A. Arrio, P. Sainctavit, C.C.D. Moulin, T. Mallah, M. Verdaguer, E. Pellegrin, C.T. Chen, J. Am. Chem. Soc. 118 (1996) 6422.
[68] V. Briois, C.C.D. Moulin, P. Sainctavit, C. Brouder, A.M. Flank, J. Am. Chem. Soc. 117 (1995) 1019.
[69] M.A. Arrio, A. Scuiller, P. Sainctavit, C.C.D. Moulin, T. Mallah, M. Verdaguer, J. Am. Chem. Soc. 121 (1999) 6414.
[70] C.C.D. Moulin, F. Villain, A. Bleuzen, M.A. Arrio, P. Sainctavit, C. Lomenech, V. Escax, F. Baudelet, E. Dartyge, J.J. Gallet, M. Verdaguer, J. Am. Chem. Soc. 122 (2000) 6653.
[71] G. Vanko, ESRF Highlights 2002, 2003, p. 59.
[72] E.C. Wasinger, F.M.F. de Groot, B. Hedman, K.O. Hodgson, E.I. Solomom, J. Am. Chem. Soc. 125 (2003) 12894.
[73] K. Okada, J. Kawai, A. Kotani, Phys. Rev. B 48 (1993) 10733.
[74] P. Glatzel, L. Jacquamet, U. Bergmann, F.M.F. De Groot, S.P. Cramer, Inorg. Chem. 41 (2002) 3121.
[75] G. Peng, F.M.F. Degroot, K. Hamalainen, J.A. Moore, X. Wang, M.M. Grush, J.B. Hastings, D.P. Siddons, W.H. Armstrong, O.C. Mullins, S.P. Cramer, J. Am. Chem. Soc. 116 (1994) 2914.
[76] X. Wang, F.M.F. Degroot, S.P. Cramer, Phys. Rev. B 56 (1997) 4553.
[77] F.M.F. Degroot, S. Pizzini, A. Fontaine, K. Hamalainen, C.C. Kao, J.B. Hastings, Phys. Rev. B 51 (1995) 1045.
[78] F.M.F. Degroot, S. Pizzini, A. Fontaine, K. Hamalainen, C.C. Kao, J.B. Hastings, Physica B 209 (1995) 763.
[79] M. Saes, C. Bressler, R. Abela, D. Grolimund, S.L. Johnson, P.A. Heimann, M. Chergui, Phys. Rev. Lett. 90 (2003) 47403.